High-energy synchrotron flares powered by strongly radiative relativistic magnetic reconnection: 2D and 3D PIC simulations

K. M. Schoeffler [1,2]★ T. Grismayer,[1] D. Uzdensky[3] and L. O. Silva[1]

[1]*GoLP/Instituto de Plasmas e Fusão Nuclear, Instituto Superior Técnico, Universidade de Lisboa, P-1049-001 Lisboa, Portugal*
[2]*Institut für Theoretische Physik, Ruhr-Universität Bochum, Bochum 44801, Germany*
[3]*Center for Integrated Plasma Studies, Physics Department, University of Colorado, Boulder, CO 80309, USA*

ABSTRACT

The time evolution of high-energy synchrotron radiation generated in a relativistic pair plasma energized by reconnection of strong magnetic fields is investigated with 2D and 3D particle-in-cell (PIC) simulations. The simulations in this 2D/3D comparison study are conducted with the radiative PIC code OSIRIS, which self-consistently accounts for the synchrotron radiation reaction on the emitting particles, and enables us to explore the effects of synchrotron cooling. Magnetic reconnection causes compression of the plasma and magnetic field deep inside magnetic islands (plasmoids), leading to an enhancement of the flaring emission, which may help explain some astrophysical gamma-ray flare observations. Although radiative cooling weakens the emission from plasmoid cores, it facilitates additional compression there, further amplifying the magnetic field B and plasma density n, and thus partially mitigating this effect. Novel simulation diagnostics utilizing 2D histograms in the n-B space are developed and used to visualize and quantify the effects of compression. The n-B histograms are observed to be bounded by relatively sharp power-law boundaries marking clear limits on compression. Theoretical explanations for some of these compression limits are developed, rooted in radiative resistivity or 3D kinking instabilities. Systematic parameter-space studies with respect to guide magnetic field, system size, and upstream magnetization are conducted and suggest that stronger compression, brighter high-energy radiation, and perhaps significant quantum electrodynamic effects such as pair production, may occur in environments with larger reconnection-region sizes and higher magnetization, particularly when magnetic field strengths approach the critical (Schwinger) field, as found in magnetar magnetospheres.

Key words: magnetic reconnection – radiation: dynamics – relativistic processes – stars: magnetars – (transients:) gamma-ray bursts.

1 INTRODUCTION

Bright, rapid gamma-ray flares occur throughout the cosmos, coming from sources associated with relativistic compact objects – neutron stars and black holes – both in our own Galaxy and beyond. Among extragalactic flaring gamma-ray sources, perhaps the most spectacular ones are gamma-ray bursts (GRBs) observed at cosmological distances: both long (several seconds) GRBs resulting from violent, explosive deaths of very massive stars, and short (≤2 s) GRBs from neutron-star mergers (Piran 2005; Mészáros 2006; Berger 2014), including the recently observed relatively weak short GRB associated with the gravitational-wave event GW-170817 detected by LIGO (Abbott et al. 2017; Goldstein et al. 2017; D'Avanzo et al. 2018). Another important class of powerful extragalactic sources flaring violently in the gamma-ray band is coronae and relativistic jets of active galactic nuclei (AGNs) powered by accreting supermassive black holes residing at the centres of many galaxies, such as M87. For example, ultrarapid (∼ 10 min) Very-High-Energy (VHE) TeV flares are observed by ground-based Cerenkov telescopes from M87

(Abramowski et al. 2012) and from many blazars (relativistic AGN jets pointing directly along our line of sight) (Aharonian et al. 2007; Albert et al. 2007b; Aleksić et al. 2011; Madejski & Sikora 2016); blazars are also observed to have simultaneous GeV flares on 1-d time-scales (Tanaka et al. 2011). Some of the most notable manifestations of variable gamma-ray activity from Milky Way sources include pulsed broad-band high-energy emission (peaking in the GeV range) from young pulsars such as Crab and Vela (see e.g. Philippov & Kramer 2022, for a recent review); the enigmatic day-long 100 MeV–1 GeV flares from the Crab pulsar wind nebula (PWN) (Abdo et al. 2011; Tavani et al. 2011; Buehler & Blandford 2014); very short and intense hard-X-ray and soft gamma-ray flares from magnetars (e.g. Mazets et al. 1999; Palmer et al. 2005; see Kaspi & Beloborodov 2017 for a recent review); and non-thermal high-energy emission extending at least up to MeV energies from accreting stellar-mass black holes in X-ray Binaries (XRBs) such as Cyg X-1 (Remillard & McClintock 2006; Zdziarski, Lubiński & Sikora 2012), which also sometimes exhibit VHE (≥100GeV) hour-long flares (Albert et al. 2007a).

The leading radiation mechanisms responsible for these flares can be either synchrotron or inverse-Compton (IC), depending on the source. Thus, in neutron-star systems, the magnetic fields are strong

★ E-mail: kevin.schoeffler@tecnico.ulisboa.pt

and the radiation is often dominated by synchrotron emission, even in the gamma-ray range. For sufficiently strong fields, the radiation emission takes place in the discrete, quantum-electrodynamic (QED) regime, where the emission of a single photon causes a significant drop in the emitting particle's energy. Moreover, the interaction of the emitted energetic gamma-ray photons with the ambient strong magnetic field can lead to electron–positron pair production, thus providing an important source of pair plasma populating the neutron-star magnetosphere. These QED processes are especially important for magnetars – young neutron stars with ultrastrong magnetic fields exceeding the QED (Schwinger) field, $B_Q \equiv m_e^2 c^3 / e\hbar \simeq 4.4 \times 10^{13}\,\mathrm{G} = E_Q$ (in Gaussian units) (e.g. Duncan & Thompson 1992). In contrast, in environments with weaker magnetic fields, e.g. those around rapidly accreting black holes (e.g. in coronae of XRBs and quasars), radiative cooling is often dominated by IC scattering (Albert et al. 2007a), which may also sometimes happen in the QED Klein-Nishina regime and power prodigious pair production (Beloborodov 2017; Mehlhaff et al. 2020).

In all of these cases, magnetic reconnection provides an attractive mechanism for explaining the high-energy flares (Romanova & Lovelace 1992; Lyubarskii 1996; Di Matteo 1998; Lyutikov 2003; Jaroschek, Lesch & Treumann 2004; Giannios 2008; Giannios, Uzdensky & Begelman 2009; Giannios 2010; Nalewajko et al. 2011; Uzdensky 2011; Uzdensky, Cerutti & Begelman 2011; Cerutti, Uzdensky & Begelman 2012; McKinney & Uzdensky 2012; Nalewajko et al. 2012; Cerutti et al. 2013; Giannios 2013; Uzdensky & Spitkovsky 2014; Sironi, Petropoulou & Giannios 2015; Cerutti, Philippov & Spitkovsky 2016; Beloborodov 2017; Lyutikov et al. 2018; Philippov & Spitkovsky 2018; Werner et al. 2018a; Werner, Philippov & Uzdensky 2018b; Giannios & Uzdensky 2019; Mehlhaff et al. 2020; Chen, Uzdensky & Dexter 2023; Hakobyan, Philippov & Spitkovsky 2023a; Hakobyan, Ripperda & Philippov 2023b). During reconnection, free energy contained in oppositely directed magnetic fields is rapidly converted to bulk flows, plasma heating, and non-thermal particle acceleration; moreover, in strongly radiative cases much of this energy is promptly converted into radiation. Furthermore, reconnecting current sheets are unstable to the secondary tearing instability leading to the generation of magnetic islands (plasmoids), or flux ropes in 3D (Loureiro, Schekochihin & Cowley 2007; Bhattacharjee et al. 2009; Uzdensky, Loureiro & Schekochihin 2010). As the freshly energized plasma tends to accumulate inside these islands, bursts of radiation are expected to be emitted from there (Cerutti et al. 2013; Giannios 2013; Petropoulou, Giannios & Sironi 2016; Sironi, Giannios & Petropoulou 2016; Beloborodov 2017; Schoeffler et al. 2019; Sironi & Beloborodov 2020).

Magnetic reconnection is therefore a potential cause of observed gamma-ray and X-ray flares. Several previous radiative-PIC studies have investigated reconnection with radiative cooling due to inverse Compton scattering, where energetic particles upscatter soft photons from an ambient radiation bath (Werner et al. 2018b; Mehlhaff et al. 2020; Sironi & Beloborodov 2020; Sridhar, Sironi & Beloborodov 2021). However, in reconnection regimes with strong magnetic fields, especially found near pulsars and magnetars, the radiation cooling is predominantly caused by synchrotron emission (Lyubarskii 1996; Uzdensky & Spitkovsky 2014; Cerutti et al. 2016). Relativistic collision-less reconnection with synchrotron cooling has been studied with radiative-PIC simulations, mostly in 2D, in a number of previous works (Jaroschek & Hoshino 2009; Cerutti et al. 2013, 2014a; Nalewajko, Yuan & Chruślińska 2018; Hakobyan, Philippov & Spitkovsky 2019; Schoeffler et al. 2019; Hakobyan et al. 2023b). It will also be the focus of this paper, which will be

devoted to studying the interplay between 3D and radiative cooling effects.

In our previous 2D computational study (Schoeffler et al. 2019), reconnection was shown to cause a sudden jump in the radiation emission. The reconnection process leads to plasma heating and non-thermal particle acceleration, both directly by the reconnecting electric field, and by the evolution and merging processes of the plasmoids. Increased plasma density, magnetic field, and temperature, caused by the compression of islands in 2D, leads to stronger emission of radiation. Radiative cooling was shown to further enhance the compression and subsequent radiation at the cores of magnetic islands. In a strong magnetic field, the enhanced radiation can reach into the gamma-ray band, potentially inducing QED effects such as pair production (Schoeffler et al. 2019).

The intriguing results of our previous 2D computational study (Schoeffler et al. 2019) naturally lead to an important question of whether the observed very strong compression effects will still occur in a more realistic 3D system. Building up on that study, in this paper we will show that enhanced compression is indeed possible in 3D at some level, and hence 3D relativistic magnetic reconnection in strong magnetic fields could still explain the occurrence of gamma-ray flares in astrophysical systems. However, the maximum degree of compression achievable in 3D remains rather modest, as compressing flux ropes tend to get disrupted by the kink instabilities. A moderate out-of-plane (the so-called 'guide') magnetic field can stabilize the kink and helps keep the plasma from escaping the flux ropes. However, at the same time, the magnetic pressure of this same guide field resists and limits the compression. It turns out that the compression is maximized for moderate values of the guide field, comparable to the upstream reconnecting field.

In this paper, we conduct a large, comprehensive study using 2D and 3D particle-in-cell (PIC) simulations using the OSIRIS framework (Fonseca et al. 2002). First and foremost, we look at the importance of 3D effects on these reconnecting systems with strong fields, which has not yet been thoroughly investigated in dedicated radiative-PIC simulation studies (see however Cerutti et al. 2014a). Furthermore, we have developed novel numerical diagnostic tools to characterize and understand in detail the plasma and magnetic field compression in magnetic islands and the emission of radiation in these reconnection regimes. This includes 2D histograms characterizing the spatial correlations between plasma density, magnetic field strength, and plasma temperature, which help us elucidate the degrees of compression that enhance the radiation emission. Extensive exploration of various broad parameter spaces elucidates the conditions under which gamma-ray flares can be expected.

This paper is organized as follows. In Section 2 we will introduce the numerical setup for our 2D and 3D radiative PIC simulations that will be presented throughout this paper. In Section 3 we will introduce the new diagnostics used to examine the emission of radiation, divided into (i) the different estimates of the total radiated power and of the local emissivity as a function of space and (ii) 2D correlation histograms of the density, magnetic field, and temperature, which help quantify the degree of compression and spatial correlations between these quantities. In Section 4 we will examine 2D simulations utilizing these new diagnostics considering different synchrotron cooling strengths characterized by different values of the normalized reconnecting magnetic field B_0/B_Q. In Section 5 we will present and analyse the results of full 3D simulations. In Section 6 we will present a broad parameter-space study exploring the effects of several important system parameters, such as the guide magnetic field, the system size and aspect ratio, and the upstream plasma magnetization. Finally, in Section 7 we

will summarize the conclusions found in this work, and discuss how magnetic reconnection in strong fields may power radiation observed in astrophysical gamma-ray flares. We also include appendices with a more detailed description of the setup in Appendix A, a more developed explanation of the theoretical boundaries of density in the density-magnetic field histograms in Appendix B, a derivation of an effective resistivity due to synchrotron radiation in Appendix C, and an associated theoretical boundary of magnetic fields in the density-magnetic field histograms in Appendix D.

2 NUMERICAL SETUP

We conducted both 2D and 3D PIC studies of relativistic reconnection in a pair plasma, taking advantage of the OSIRIS framework (Fonseca et al. 2002). OSIRIS self-consistently includes synchrotron radiation and the QED process of pair production by a single gamma-ray photon propagating across a strong electromagnetic field (Grismayer et al. 2016, 2017). However, in this study, we look at a regime where, although the back-reaction caused by the synchrotron radiation plays an important role, the QED processes are not relevant. In these simulations, we track the total amount of radiated energy emitted by each particle at every time-step and use the local estimation for the emissivity ϵ_{est} (described in Section 3.1) to track emission as a function of space and time.

We simulate an initial double relativistic Harris current-sheet equilibrium (Harris 1962; Kirk & Skjæraasen 2003) with periodic boundary conditions, which is explained in more detail in Appendix A. For our simulations presented in Sections 4 and 5, we focus on the fiducial values of the key system parameters described in this section, while we will vary some of them in the parameter scans in Section 6.

The computational domain is initially filled with a relativistically hot Maxwell-Jüttner background electron–positron plasma with uniform density (of each species) n_b and temperature $T_b = 4 m_e c^2$. These parameters are chosen to yield a high upstream 'hot' plasma magnetization

$$\sigma_h \equiv \frac{B_0^2}{4\pi (2n_b) h_b} = 25.76, \tag{1}$$

where B_0 is the reconnecting magnetic field oriented along the $\hat{x}$ direction and h_b is the relativistic enthalpy per particle in the upstream background ($h \approx 4T$ for ultrarelativistic temperatures). This corresponds to an upstream plasma beta $\beta_{up} \equiv 8\pi (2n_b) T_b / B_0^2 = 1/2\sigma_h = 0.0202$. Note that the value of magnetization adopted in this paper is greater than the value $\sigma_h = 6.44$ of our previous work (Schoeffler et al. 2019). We also include an out-of-plane ($\hat{z}$) uniform guide magnetic field $B_G = 0.4 B_0$. The cold magnetization, discussed in Appendix A, is $\sigma_c \equiv B_0^2 / 4\pi (2n_b) m_e c^2 = 412$.

In addition to the uniform background, we include two antiparallel initial Harris current layers, each lying in a $y = const$ plane and carrying electric current in the $\pm \hat{z}$ direction. The layers are composed of drifting Maxwell-Jüttner distributions of counterstreaming electrons and positrons with central density (of each species) $n_0 = 37 n_b$, rest-frame temperature $T_0 = 6.92 m_e c^2$, an initial half-thickness $\delta = 2.55 \rho_L$, and a drift velocity $v_d/c = 0.56$ for each species (Lorentz factor $\gamma_d = 1.21$, proper velocity $u_d = \gamma_d v_d/c = 0.68$).

Here, our main fiducial normalizing length scale

$$\rho_L \equiv \gamma_T m_e c^2 / e B_0 = \gamma_T c / \Omega_c \tag{2}$$

is defined as the Larmor radius of a background particle with a Lorentz factor corresponding to the peak of the initial upstream relativistic Maxwell-Jüttner distribution, $\gamma_T \equiv 2T_b / m_e c^2$. Here, Ω_c

$\equiv e B_0 / m_e c$ is the classical (non-relativistic) gyrofrequency. Other important length scales include the respective background (non-relativistic) skin depth $d_e \equiv [m_e c^2 / 4\pi (2n) e^2]^{1/2}$ and Debye length $\lambda_D \equiv [T/4\pi (2n) e^2]^{1/2}$, defined by the initial background plasma parameters ($n = n_b$ and $T = T_b$):

$$d_e = \rho_L \left(\sigma_h m_e c^2 / T_b\right)^{1/2} \approx 2.53 \rho_L, \tag{3}$$

$$\lambda_D = \rho_L \sigma_h^{1/2} \approx 5.08 \rho_L, \tag{4}$$

both of which are larger than ρ_L, scaling as $\sigma_h^{1/2} \rho_L$ for relativistic temperatures. We can also introduce the values of these length scales in the Harris sheet where $n = n_0$ and $T = T_0$:

$$\rho_{L,H} = \rho_L \left(T_0/T_b\right) \approx 1.73 \rho_L, \tag{5}$$

$$d_{e,H} = \rho_L \left(\sigma_h n_b m_e c^2 / n_0 T_b\right)^{1/2} \approx 0.42 \rho_L, \tag{6}$$

$$\lambda_{D,H} = \rho_L \left(\sigma_h n_b T_0 / n_0 T_b\right)^{1/2} \approx 1.10 \rho_L. \tag{7}$$

The Larmor radius and Debye length in the reconnection regions increase as time progresses, due to the heating of the plasma. Our fiducial simulation domain size is $2L_x \times 2L_y (\times 2L_z) = 628.8\rho_L \times 628.8\rho_L (\times 117.2\rho_L)$ in 2D (3D), and the simulations are run for about 3.16 light crossing times L_y/c ($t_{max} = 7948 \Omega_c^{-1}$).

Our typical 2D (3D) simulation domain size consists of $1280 \times 1280 (\times 240)$ computational grid cells of size $\Delta x = \Delta y (= \Delta z) = 0.49\rho_L$, initially with 16 (8) particles per species in each cell, with a total of about 9.0×10^7 (1.0×10^{10}) particles. There are thus about 1700 (8900) initial macroparticles per Debye cube in the background plasma. Although initially there are only ∼80 (90) macroparticles per Debye cube in the Harris sheet, once the background plasma enters the reconnection region, this number becomes much larger. The simulations are typically run with a time-step of $\Delta t = 0.5\Delta x/c = 0.25\rho_L/c = 0.25\gamma_T \Omega_c^{-1}$.

A novel feature of our simulations is the self-consistent inclusion of optically thin radiation emission by relativistic particles due to strong magnetic fields. Depending on the importance of QED effects, OSIRIS can treat radiation emission with two alternative implementations: a continuous description of classical radiation reaction, and a quantized description that includes the QED processes.

To determine whether QED (discrete-emission) effects are important for a given emitting particle, we calculate the relativistic invariant for an electron (or positron) of energy $\gamma m_e c^2$ and momentum $\boldsymbol{p}$ moving in an electromagnetic field

$$\chi_e = \frac{1}{B_Q} \sqrt{\left(\gamma \boldsymbol{E} + \frac{\boldsymbol{p}}{m_e c} \times \boldsymbol{B}\right)^2 - \left(\frac{\boldsymbol{p}}{m_e c} \cdot \boldsymbol{E}\right)^2}, \tag{8}$$

which in our parameter regimes, where usually $B \gg E$, can be approximated by

$$\chi_e \approx \frac{\gamma B}{B_Q}. \tag{9}$$

As this parameter increases, the particle will emit higher energy photons, and, once χ_e approaches 1, QED effects including discrete gamma-ray emission, and, for even higher χ_e, pair production, can start playing an important role. However, in the simulations presented in this paper, the χ_e parameter does not usually reach significantly high values even for very energetic particles (i.e. $\chi_e \lesssim 1$). We thus use the continuous description, with the radiation back-reaction accounted for classically using the Landau-Lifshitz model (Landau & Lifshitz 1975) for the radiative drag force, while we keep track of the total radiated energy.

The radiative cooling is significant when the synchrotron cooling time $\sim (\alpha_{\rm fs} \chi_e \Omega_c)^{-1}$, where $\alpha_{\rm fs} \equiv e^2/\hbar c \approx 1/137$ is the fine structure constant, is shorter than or comparable to the relevant time-scale of the simulation, i.e. a few global light crossing times ($t_{\rm max} \approx 3.16 L_y/c$). After one light crossing time L_y/c, a relativistic particle with energy $\gamma m_e c^2$ moving in a magnetic field B experiences significant cooling (i.e. loss of a significant fraction of its energy) when

$$\frac{2}{3} \alpha_{\rm fs} \chi_e \Omega_c \frac{L_y}{c} = 2\gamma \frac{B^2}{B_0^2} \ell_B > 1, \qquad (10)$$

a parameter directly related to the global magnetic compactness

$$\ell_B \equiv \sigma_T L_y \frac{U_{B0}}{m_e c^2}. \qquad (11)$$

Here, σ_T is the Thomson cross-section, and $U_{B0} = B_0^2/8\pi$ is the initial upstream magnetic energy density. Note that in our fiducial set of simulations, with fixed values of $L_y/\rho_L = 314.4$ and $\gamma_T = 2T_b/m_e c^2 = 8$, the compactness ℓ_B scales just linearly (instead of quadratically) with B_0, since $\rho_L = \gamma_T m_e c^2/eB_0 \propto B_0^{-1}$.

We assume that synchrotron emission is the dominant radiation mechanism. For the simulation parameters adopted in this study, the Thomson optical depth is $\tau_T \equiv \sigma_T L_y n_b = 1.35 \times 10^{-4}$, and thus the radiation occurs in an optically thin regime. Here we ignore the IC scattering of both the synchrotron photons (i.e. synchrotron self-Compton, SSC) and any possible ambient photons of external origin (i.e. external IC); we also neglect synchrotron self-absorption; investigating the effect of these additional radiative processes is left for future studies.

For reference, we define the characteristic radiation-reaction limit Lorentz factor $\gamma_{\rm rad}$ described (e.g. in Uzdensky et al. 2011; Uzdensky 2016; Werner et al. 2018b; Mehlhaff et al. 2020; Sironi & Beloborodov 2020; Mehlhaff et al. 2021). This factor is defined as the particle Lorentz factor for which the radiation-reaction force is equal to the acceleration force by the reconnecting electric field $E_{\rm rec} = \beta_E B_0$, or, equivalently, the particle's radiative cooling time is approximately equal to the gyro-period. For synchrotron radiation, this limit is

$$\gamma_{\rm rad}^2 = \frac{1}{\sin^2 \alpha} \frac{3}{2} \frac{\beta_E}{\alpha_{\rm fs}} \frac{B_Q}{B_0} = \frac{1}{2\ell_B} \frac{\Omega_c L_y}{c} \frac{\beta_E}{\sin^2 \alpha} = \frac{4\pi e}{\sigma_T B_0} \frac{\beta_E}{\sin^2 \alpha}, \quad (12)$$

where $\beta_E \sim 0.1$ is the dimension-less reconnection rate (reconnection inflow velocity normalized to the speed of light), and α is the particle's pitch angle with respect to the magnetic field.

In order to investigate the effects of radiative cooling, in this paper we present the results (in both 2D, Section 4, and 3D, Section 5) from three simulations with different cooling strengths. The cooling strength is controlled by varying the reconnecting magnetic field strength, using the same magnetic field values as those used by Schoeffler et al. (2019):

(i) Classical Case: $B_0/B_Q = 4.53 \times 10^{-6}$ (i.e. $B_0 = 2 \times 10^8$ G), where the peak local average value of χ_e reaches $\chi_e \sim 0.0003 \ll (\alpha_{\rm fs} \Omega_c t_{\rm max})^{-1} \approx 0.017$, and $2\gamma(B/B_0)^2 \ell_B \approx 0.004$ ($\ell_B \approx 2 \times 10^{-5}$), and hence cooling is not important;

(ii) Intermediate Case: $B_0/B_Q = 4.53 \times 10^{-4}$ ($B_0 = 2 \times 10^{10}$ G), where $(\alpha_{\rm fs} \Omega_c t_{\rm max})^{-1} \approx 0.017 < \chi_e \sim 0.03 \ll 1$, and $2\gamma(B/B_0)^2 \ell_B \approx 0.4$ ($\ell_B \approx 0.002$), and cooling is becoming important;

(iii) Radiative Case: $B_0/B_Q = 4.53 \times 10^{-3}$ ($B_0 = 2 \times 10^{11}$ G), where $\chi_e \sim 0.3$, and $2\gamma(B/B_0)^2 \ell_B \approx 4$ ($\ell_B \approx 0.02$), and cooling is very important.

In these estimations, e.g. of $\chi_e(B, \gamma)$, to evaluate peak local average values inside of magnetic islands/flux ropes, we have assumed that

the magnetic field is enhanced by a factor of about 1.5 (i.e. $B \approx 1.5 B_0$) and the temperature by a factor of 5 (i.e. $T \approx 5 T_b$, $\gamma \approx 5\gamma_T$). Furthermore, assuming a normalized reconnection rate $\beta_E = 0.1$ and pitch angle $\alpha = 90°$, these parameters correspond to $\gamma_{\rm rad} \simeq 2000$, 200, and 60, respectively. For the radiative case, in order to keep the initial upstream plasma from cooling substantially in the course of the simulation, we restrict the degree of radiative cooling based on the background parameters to $2\gamma_T \ell_B \approx 0.44$, with a background average $\chi_e(B_0, \gamma_T) \approx 3.6 \times 10^{-2}$. However, as the system evolves, regions develop with an average local value $\chi_e \approx 0.3$ (as shown in Section 6.4), and energetic particles occur with $\chi_e \approx 1$, allowing for significant local cooling. Note, however, that unlike in Ref. Schoeffler et al. (2019), these values of χ_e are small enough that there are no significant QED effects (such as discrete photon emission and pair creation). Nevertheless, we still expect qualitatively similar results; negligible cooling in the classical case, and a significant radiated fraction of the released magnetic energy, in part due to a strong enhancement of magnetic island compression, in the radiative case and, to a lesser extent, in the intermediate case.

In Section 6, we also explore the parameter space starting with our 3D radiative case $B_0/B_Q = 4.53 \times 10^{-3}$, and varying B_G/B_0, L_z/ρ_L, L_y/ρ_L, and σ_h.

3 DIAGNOSTICS

3.1 Estimated radiated power and emissivity

While it is possible to do *in-situ* measurements in reconnection experiments and even in the Earth's magnetosphere using spacecraft, for phenomena that take place around remote astrophysical objects like neutron stars, the only data that can be obtained comes from observations of radiation. We thus pay special attention to diagnostics measuring the radiation emitted in these environments both as a function of time and of space.

Each particle emits radiation at any given moment in time with a power that is a function of χ_e and, in the classical regime ($\chi_e \ll 1$), can be expressed as

$$P = \frac{2}{3} \frac{\alpha_{\rm fs} m_e c^2}{t_C} \chi_e^2 \approx \frac{2}{3} \frac{e^2}{c} \gamma^2 \Omega_c^2 \sin^2 \alpha, \qquad (13)$$

where the second expression, for classical synchrotron radiation, is valid as long as the magnetic field is much stronger than the electric field. Here $t_C = \hbar/m_e c^2 \approx 1.29 \times 10^{-21}$s is the electron Compton time.

While the total power emitted in a given optically thin system is calculated by summing the powers P radiated by each particle, it is also useful to study the location in space where the radiative power is emitted from. Instead of considering a discrete sum of particles, one can consider a 6D distribution of particles $f(\boldsymbol{p}, \boldsymbol{x})$ over the momentum space $\boldsymbol{p}$ and the coordinate space $\boldsymbol{x}$, and calculate P as a function of $\boldsymbol{p}$, $\boldsymbol{B}(\boldsymbol{x})$, and $\boldsymbol{E}(\boldsymbol{x})$. Then, the total power emitted at a given moment in time can be expressed as:

$$P_{\rm tot} = \int \mathrm{d}^3 p \, \mathrm{d}^3 x \, f(\boldsymbol{p}, \boldsymbol{x}) P(\boldsymbol{p}, \boldsymbol{x}) = \int \mathrm{d}^3 x \, \epsilon(\boldsymbol{x}), \qquad (14)$$

where the local emissivity

$$\epsilon(\boldsymbol{x}) \equiv \int \mathrm{d}^3 p \, f(\boldsymbol{p}, \boldsymbol{x}) P(\boldsymbol{p}, \boldsymbol{x}) \qquad (15)$$

is the power emitted from a unit volume in space. The total power is thus proportional to the volume-averaged emissivity $P_{\rm tot} \sim \langle \epsilon(\boldsymbol{x}) \rangle$, where the angle brackets represent an average over space. In our

simulations, we calculate P_{tot} at each time-step by summing the radiation from all the particles in the simulation. We normalize P_{tot} to its initial value $P_{tot, 0}$, $\bar{P}_{tot} \equiv P_{tot}/P_{tot, 0}$, in order to emphasize the relative enhancement of radiation due to reconnection.

In principle, in PIC simulations it is possible to precisely measure both P_{tot} and ϵ by summing the power emitted by each particle within each given small volume element, e.g. in each grid cell. However, in MHD simulations, for example, the details of the particle distribution are not available. Furthermore, only limited data are available in observations. We will thus explore several fluid-level methods of estimating P_{tot} using various assumptions, and check their fidelity by comparing them with our exact kinetic measurements.

Although we do not introduce a diagnostic for the precise (particle-based) value of $\epsilon(\boldsymbol{x}, t)$ in our simulations, we will define a reasonable fluid-based method of estimation where we assume a local isotropic Maxwell-Jüttner distribution in the comoving frame corresponding to the local drift velocity $\boldsymbol{v}_d$ of each species.

To obtain the effective local temperature from a time-evolving distribution that is not necessarily Maxwell-Jüttner, we take the temperature tensor $T_{ij} \equiv m_e^{-1} \int d^3 p \, (p_i p_j/\gamma) f(\boldsymbol{p})/\int dp^3 \, f(\boldsymbol{p})$ for the background electron species calculated in its local rest frame [i.e. in the so-called Eckart frame (Eckart 1940), where the local current of that species vanishes]. Here, p_i is the ith component ($i = x, y, z$) of the momentum, $\gamma = \sqrt{1 + p^2/m_e^2 c^2}$, and $f(\boldsymbol{p})$ is the momentum distribution function. The effective temperature is then defined using the trace of the temperature tensor, $T \equiv Tr(T_{ij})/3$. While this temperature initially only represents the temperature of the background plasma, as the background population mixes with the current-sheet population, this temperature becomes a representative temperature of the system. We also define a representative density n, which is the total local particle density of one species (e.g. positrons), including both initially background and Harris current-sheet particles.

Assuming again that $E \ll B$, we can say that $\chi_e \approx \gamma B/B_Q$, and substitute equation (13) into equation (15) to get an estimate for the emissivity. Based on our assumption of an isotropic Maxwell-Jüttner distribution in the local comoving frame, we can integrate over the pitch angles α and momenta, the result of which is proportional to $B_\perp^2 [1 + u_d^2(\boldsymbol{x})] + B_\parallel^2$. Here, $\boldsymbol{B}_\parallel$ and $\boldsymbol{B}_\perp$ are defined with respect to the local bulk fluid velocity $\boldsymbol{v}_d(\boldsymbol{x})$ of the given species, and $u_d(\boldsymbol{x}) \equiv \gamma_d v_d/c$ is the fluid's local normalized proper velocity, with γ_d being the corresponding Lorenz factor. For simplicity, we will not include in our estimation the Doppler-boosting enhancement in radiated power based on u_d, whose direction may be difficult to determine in observations. We, therefore, find the following estimation only in terms of local, space-dependent parameters $n(\boldsymbol{x})$, $T(\boldsymbol{x})$, and $B(\boldsymbol{x})$:

$$\epsilon_{est}(\boldsymbol{x}) \equiv \frac{16}{3} \frac{e^4}{m_e^4 c^7} \left[2n(\boldsymbol{x})\right] T^2(\boldsymbol{x}) B^2(\boldsymbol{x}). \tag{16}$$

Note that while this estimate is calculated in the lab frame, the expression takes the temperature variable calculated in the comoving (Eckart) frame. The factor of 2 in front of the density represents the two species, electrons and positrons. We normalize ϵ_{est} to the initial background plasma value $\epsilon_{est, 0}$, evaluated with $T = T_b$, $B^2 = B_0^2 + B_G^2$, and $n = n_b$. The contribution of the background plasma to the initial total normalized estimated radiation power is $P_{back, 0} \equiv \int d^3 x \, \epsilon_{est, 0} \approx 0.41 P_{tot, 0}$, with all the simulations performed using the fiducial parameters described in Section 2. (The overall effect of the weaker magnetic field at the centre of the current sheets is negligible.) We also calculated the initial total normalized estimated radiation power due to the Harris sheet: $P_{HS, 0} \equiv \int d^3 x \, \epsilon_{est, HS} \approx 0.59 P_{tot, 0}$, where $\epsilon_{est, HS}$ is ϵ_{est} evaluated with

$T = T_0$, $B^2 = B_x^2(y)(1 + 3u_d^2) + B_G^2$, and $n = n(y) - n_b$. Here, in order to get a more accurate estimate of the initial emissivity, we account for the drifts perpendicular to the magnetic field by including the additional factor of $1 + 3u_d^2$, where u_d is the proper speed of the drifting particle populations in the initial Harris current layer, as defined in Section 2. The radiation from the two populations thus accounts for all of the initial radiation $P_{tot, 0} \approx P_{back, 0} + P_{HS, 0}$.

Our first simplified estimate of the total radiated power P_{tot} at any given moment in time is defined as

$$P_{tot, est} \equiv P_{back, 0} \left\langle \frac{n}{n_b} \frac{T^2}{T_b^2} \frac{B^2}{B_0^2 + B_G^2} \right\rangle, \tag{17}$$

and is calculated by substituting equation (16) into equation (14). Here, $<...>$ is the volume-average of the product of n, T^2, and B^2 normalized to the background values: n_b, T_b^2, and $B_0^2 + B_G^2$, which are used to calculate $P_{back, 0}$. At $t = 0$, $P_{tot, est} \approx 0.49 P_{tot, 0}$. While this estimation includes the density from the Harris sheet population, it initially underestimates its radiation because the temperature diagnostic is based only on the background population. The estimation, therefore, takes into account neither the higher temperature of the initial Harris population nor the relativistic enhancement due to the bulk flows of electrons and positrons carrying the electric current. As described earlier, we have ignored the increased radiation due to the bulk flows, out of simplicity. Both the currents and, later, reconnection outflows do persist throughout the simulations. However, while the enhanced radiation due to the bulk flows does play a role (e.g. as in the minijet model of Giannios et al. 2009; Giannios 2010; see also Nalewajko et al. 2011; Giannios 2013), as we will show below, the simplified estimation of the total, bolometric radiated power remains qualitatively accurate. Regions with the highest thermal energy content (namely, large plasmoids) tend to have low bulk-flow velocities, and thus the enhancement of radiation due to the bulk flows is limited. Although the assumption of a local Maxwell-Jüttner distribution is initially accurate, this estimate ignores any kinetic effects which can play a role as the distribution evolves. Therefore, while the above estimate is reasonable for relatively steep spectra, for harder, highly non-thermal spectra the kinetic effects play an important role, especially for the high-energy emission, as we discuss in Section 4.4 and at the end of Section 5.1.

We also define an even more basic estimation for P_{tot}, making a connection to situations where one knows only the total (volume-integrated) particle kinetic energy (and hence pressure) and magnetic energy as functions of time:

$$P_{tot, est2} \equiv P_{back, 0} \left\langle \frac{nT}{n_b T_b} \right\rangle^2 \left\langle \frac{B^2}{B_0^2 + B_G^2} \right\rangle \bigg/ \left\langle \frac{n}{n_b} \right\rangle. \tag{18}$$

At $t = 0$, we find $P_{tot, est2} \approx 0.62 \, P_{tot, 0}$. This initial estimation is somewhat larger than $P_{tot, est}$ because it does not take into account the initial anticorrelation between the magnetic field and the plasma pressure due to the initial pressure balance across the current sheet. Note that this eventually becomes a positive correlation, as discussed in the next subsection. Due to the particle number conservation, as the spatial distribution of n evolves, $<n>$ remains constant in time, and so only one value is needed for calculating $P_{tot, est2}$. In cases not studied here, where a significant number of pairs are created, the time evolution of this factor would be important.

The simple estimates $P_{tot, est}$ and $P_{tot, est2}$ for the total radiated power P_{tot} provide convenient estimations from the often limited measurements available in MHD simulations or from observations. Furthermore, their comparison with the actual exact P_{tot} measured in the radiative PIC simulations helps elucidate and highlight the importance of the spatial correlation between the magnetic field
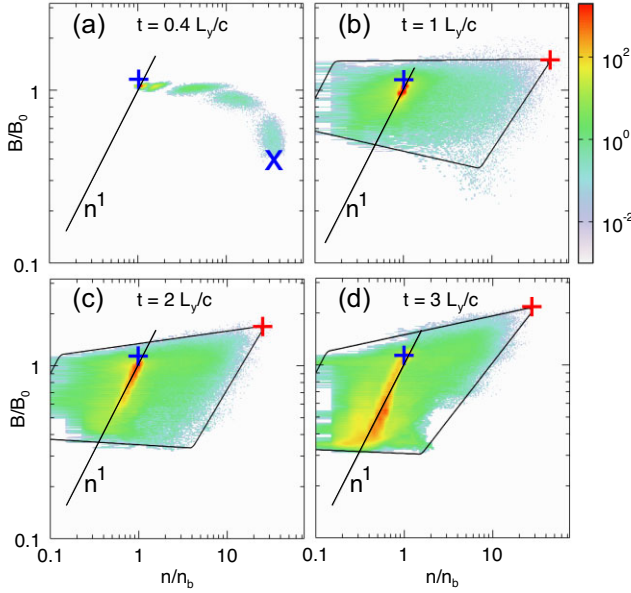
Figure 1. Histograms in log–log n-B space of the 3D radiative simulation with $B_G/B_0 = 0.4$, $L_y/\rho_L = 314.4$, and $\sigma_h = 25.76$, at 4 time-snapshots: (a) $tc/L_y = 0.4$, (b) $tc/L_y = 1$, (c) $tc/L_y = 2$, and (d) $tc/L_y = 3$. At intermediate and late times (panels b–d), the histograms exhibit clear, well-defined power-law boundaries forming 4-sided polygons. The blue plus signs mark the initial conditions of the upstream background plasma, the blue 'X' (in panel a) represents the initial conditions at the centre of the current sheet ($n/n_b = 37$, $B/B_0 = 0.4$), the red plus signs mark the upper right vertex of the best-fitting polygons, and the $B \sim n$ scaling [see equation (19)] is highlighted.

and plasma pressure and of the kinetic effects not included in the estimates. Furthermore, diagnostics showing the spatial distribution of the local estimated emissivity $\epsilon_{est}(\boldsymbol{x})$ allow us to understand better how sudden enhancements of radiation occur in the context of the reconnection process.

3.2 Parameter-space histograms

In our previous 2D work, we have argued that, due to radiative cooling, the magnetic fields and density of the plasma are strongly compressed in the cores of magnetic islands (Schoeffler et al. 2019). Although this effect enhances the radiation in these regions, in this paper we will show that it only mitigates the loss of the emitted power due to the overall cooling of the radiating particles. We will argue that the positive correlation of the magnetic fields and density inside islands leads to enhanced radiation compared to the simple estimate $P_{tot, est2}$, such that $P_{tot} \gg P_{tot, est2}$. A histogram of the grid points in the n-B space will both allow us to obtain a quantitative measure for the degree of compression and show that there is in fact a correlation between magnetic fields and density.

Therefore, we visualize this compression and correlation between n and B via the 2D distribution of simulation points in the n-B parameter space. As an illustration, in Fig. 1 we examine the histograms for the 3D radiative case taken at 0.4, 1, 2, and 3 light crossing times. We show joint 2D histograms of the local values of the normalized n/n_b and B/B_0 at each grid point. An integral of the histogram over a region of n-B space represents the fraction of the volume with the values of n and B that lie in that region.

The vast majority of the grid points are part of the upstream background, where initially $n = n_b$ and $B = \sqrt{B_0^2 + B_G^2} \approx 1.08 B_0$, indicated by the blue plus sign in Fig. 1. The background plasma is

well frozen into the magnetic field. As the upstream, unreconnected magnetic flux is depleted over time via magnetic reconnection, the upstream magnetic field, and density drop, keeping the magnetic flux $B\Delta y$ and number of particles $n\Delta y L_x$ within a given upstream flux tube of (time-changing) width Δy constant. The upstream field and density thus follow the simple ideal-MHD relation

$$\frac{B}{B_0} = \frac{n}{n_b}, \tag{19}$$

assuming there is not much variation in the $\hat{x}$ direction. This simple linear trend can be noted in Fig. 1 for $n/n_b < 1$ where the narrow orange/red band extends over time to lower values of n and B following equation (19). Aside from this basic observation, after a couple of light-crossing times for the 3D cases, the plasma from the central mid-plane of the initial Harris current sheet indicated by the blue 'X' in Fig. 1 mixes with the background plasma with the help of a kinking instability described in Section 5.2.

One of the most striking features of the histograms prominently seen at intermediate and late times is that the histograms become bounded above, below, and to the right by clear, distinct limits that can be modelled by power laws. These limits, which constrain the compression of density and magnetic field, will be further discussed in Section 5.2.

In order to better understand how the compression depends on radiative cooling strength quantified by B_0/B_Q, and on various other parameters in Section 6, we design here a novel numerical procedure for measuring the degree of compression. First, we note that, for the 3D simulations after about a light crossing time (starting at $tc/L_y = 0.85$), the boundaries of the histogram in log–log n-B space can be approximated with a best fit of a four-sided polygon. The parameters describing this polygon are first estimated by hand to match the histogram. A step function with value 1 inside the polygon, with a 20-point smooth, is compared with another step function with value 1 where the histogram is non-zero, with a 10-point smooth. The parameters of each of the lines are then optimized to a best fit (Markwardt 2009). After each time-step, the previous best fit is used as the new initial estimation.

For example, in Fig. 1, at $tc/L_y = 1, 2$, and 3, the respective slopes of the boundaries (power-law indices $B \sim n^\alpha$) are ($\alpha = 0.005, 0.075$, and 0.113) above, and (0.78, 0.88, and 0.67) to the right of the histogram. These lines cross at the points $(n/n_b, B/B_0) = (48.5, 1.53)$, (24.9, 1.71), and (28.8, 2.18) respectively, indicated by red crosses. These intersection points mark the upper right corners of the polygons and thus give us an estimation for a maximum level of both n and B. The final slopes match reasonably well with theoretical predictions that $\alpha = 1/12$, $\alpha = 1/6$, and $\alpha = 1$, which will be discussed in Section 5.

A similar histogram can be constructed for the n-T space instead of the n-B space. This diagnostic furnishes us a convenient visual tool for examining the spatial correlations between n and T.

We will be using these histogram diagnostics extensively in Sections 4.2, 4.3, 5.1, 5.2, and throughout Section 6, especially in Section 6.2.

4 2D RESULTS

In this section we will explore results from three 2D simulations with varying levels of radiation losses: the classical case $B_0/B_Q = 4.53 \times 10^{-6}$, the intermediate case $B_0/B_Q = 4.53 \times 10^{-4}$, and the radiative case $B_0/B_Q = 4.53 \times 10^{-3}$. The rest of the simulation parameters are held fixed here at their fiducial values listed in Section 2. We show the process of reconnection and the effects that radiation cooling/back-reaction has on it.
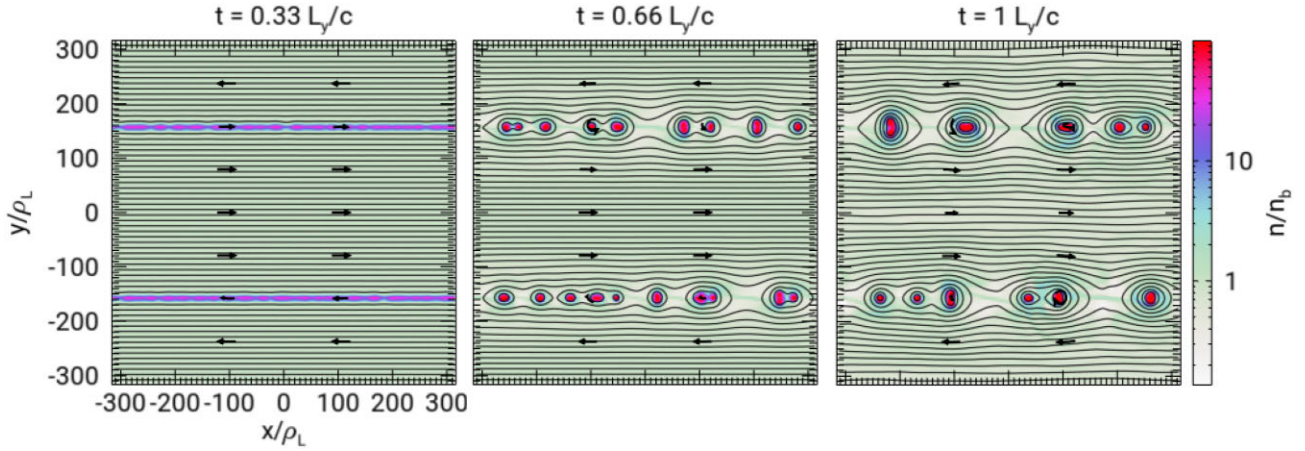
Figure 2. Maps of density with in-plane magnetic field lines overlaid for the 2D radiative case $B_0/B_Q = 4.5 \times 10^{-3}$, at (a) $t = 0.33L_y/c$, (b) $t = 0.66L_y/c$, and (c) $t = 1L_y/c$.

In all three simulations, the initial current sheet is unstable to the tearing instability, leading to the formation of multiple magnetic islands separated by X-points, where magnetic reconnection converts the upstream magnetic energy into plasma kinetic energy in the form of bulk outflows, heating, and non-thermal particle acceleration. The plasma density maps showing the current sheet with superimposed magnetic field lines (lines of constant magnetic flux), shown in three panels in Fig. 2, illustrate the generation and merging of magnetic islands during the first light crossing time (up to $t = L_y/c$) of the radiative case, which is qualitatively representative of the other cases as well.

One of the key characteristics of the magnetic reconnection process is the reconnection rate. To compute it, we first calculate the magnetic flux function $\psi \equiv \hat{z} \cdot \int \boldsymbol{B}_{xy} \times \mathrm{d}\boldsymbol{l}$, where $\boldsymbol{B}_{xy}$ is the in-plane (xy) magnetic field, and where the integral is taken over the line/contour starting at the bottom left-hand corner, going vertically along the $\hat{y}$ direction, and then horizontally along the $\hat{x}$ direction. The reconnection rate measures how fast the difference in ψ between the two current sheets decreases, multiplied by a factor of 1/2 accounting for the magnetic flux being divided between the two reconnecting current sheets. We calculate it using two measures: (i) the difference between the major X-points of the two current sheets, corresponding, respectively, to the minimum value of ψ in the upper current sheet and the maximum value of ψ in the lower current sheet (defined by the planes $y = \pm L_y/2$, where the current sheets are initially centred) and (ii) the difference between the two values calculated by averaging ψ along each current sheet (i.e. along the previously defined plane). The corresponding reconnection rates (defined as the absolute value of the time derivative of the flux) are found to be 0.25 and 0.08 $B_0 c_A$, respectively (where $c_A \approx c$ is the upstream Alfvén speed), between $tc/L_y = 0.5$ and 1, after which the rate slows down by a factor of about 4. This is consistent with the predicted reconnection rate for magnetized pair plasmas calculated by Goodbred & Liu (2022). Although there is a slight trend of decreased reconnection rate for the more radiative cases (stronger B_0/B_Q), the differences are of the same order as the error ($\sim$ 10 per cent).

The conversion of energy from the magnetic field to the kinetic energy of the plasma particles, and the subsequent conversion to radiation, is shown for all three cases in Fig. 3. Unlike the classical case, where a negligible amount of the kinetic energy is radiated away, significant energy goes to radiation in the intermediate and radiative cases, increasing with the strength of the upstream magnetic
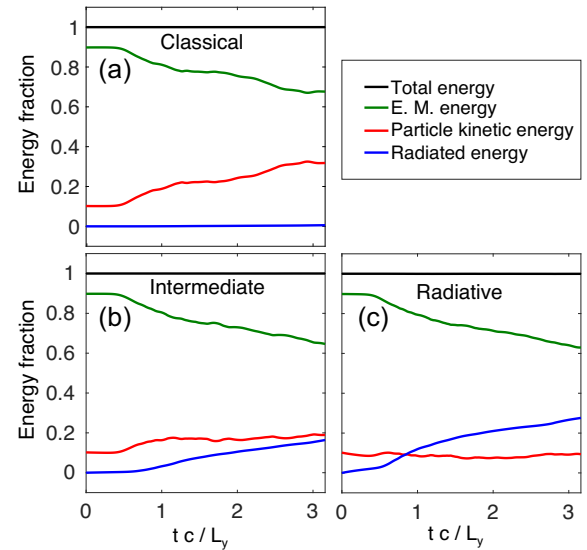

Figure 3. Time-evolution plots of energy partition between electromagnetic (green), particle kinetic (red), and radiated (blue) energies, along with their sum (black), for the 2D simulations with (a) $B_0/B_Q = 4.5 \times 10^{-6}$, (b) $B_0/B_Q = 4.5 \times 10^{-4}$, and (c) $B_0/B_Q = 4.5 \times 10^{-3}$.

field. In these cases, especially in the radiative case, the particle kinetic energy stays nearly flat throughout most of the evolution from $t \simeq 1 L_y/c$ onward, while the radiation energy steadily increases; this indicates that the particles act as efficient radiators in this case, promptly converting the energy they receive from magnetic field dissipation into radiation.

Although even in the initial state the thermal particle motion of the plasma leads to some synchrotron radiation energy losses, we will show in Section 4.1 that the radiated power P_{tot} increases rapidly and significantly during the onset of reconnection, in agreement with all estimates for P_{tot}. We will then show in Section 4.2 that, when considering the emissivity as a function of space, a positive correlation between the plasma density n and magnetic field strength B leads to an enhanced P_{tot}. Although this correlation is more prominent in more radiative cases, we will then show in Section 4.3 that the correlation between n (or B) with the temperature T becomes
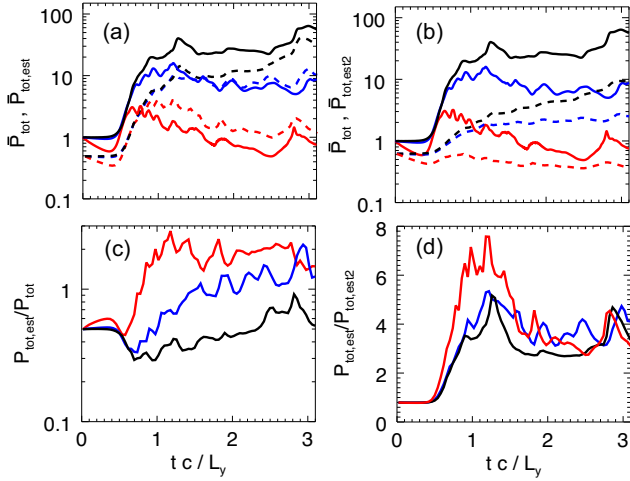
Figure 4. (a) Total normalized radiated power $\bar{P}_{tot} \equiv P_{tot}/P_{tot,0}$ (solid lines) for 2D simulations with $B_0/B_Q = 4.5 \times 10^{-6}$ (black, classical case), 4.5×10^{-4} (blue, intermediate case), and 4.5×10^{-3} (red, radiative case). These colours are used for all panels in this figure. The dashed lines represent the normalized estimated power $\bar{P}_{tot,est} \sim \langle nT^2 B^2 \rangle$ [see equation (17)]. (b) Total normalized radiated power $\bar{P}_{tot}$ (solid lines) and the second normalized power estimation $\bar{P}_{tot,est2} \sim \langle nT \rangle^2 \langle B^2 \rangle$ [see equation (18)] in dashed lines. (c) Ratio $P_{tot,est}/P_{tot}$. (d) Ratio of the two estimations of power radiated $P_{tot,est}/P_{tot,est2}$.

negative and reduces the normalized $\bar{P}_{tot}$. Finally, in Section 4.4 we will address important kinetic effects that affect the emitted power.

4.1 Total emitted power

Before discussing the enhancements of the power emitted as a result of magnetic reconnection, we should note the dependence of the radiated power per particle on the magnetic field strength B_0/B_Q (at fixed σ_h, etc.). On the one hand, as the radiated power for a given particle is proportional to B_0^2, there is the trivial effect that the most radiative cases (i.e. those with stronger B_0/B_Q) will clearly radiate much more than less radiative ones. For the radiative case, $P_{tot,0}$ is a factor of 10^2 larger than in the intermediate case and a factor of 10^6 larger than in the classical case. On the other hand, here we are interested in the relative modifications to this trivial scaling due to various factors. Therefore, we will focus the discussion in this paper on the normalized radiated power $\bar{P}_{tot} \equiv P_{tot}/P_{tot,0}$. (We will also use this bar notation when plotting estimates $\bar{P}_{tot,est}$ and $\bar{P}_{tot,est2}$, which have the same normalization.) We will show that this relative enhancement in radiation is weaker for the most radiative cases. That is, the normalized radiation is weaker, but the actual amount of radiation remains much greater.

We first examine the time evolution of the total normalized radiated power $\bar{P}_{tot}$ for all three 2D cases, which we plot in Figs 4(a) and (b) (solid lines). After $t \approx 0.5L_y/c$, magnetic reconnection gets started and the power of emission abruptly increases by a factor as high as 30. This is caused by the increase in temperature and a concentration of magnetic fields inside magnetic islands discussed in Section 4.2.

The major effect of stronger radiative cooling, quantified by B_0/B_Q, is a drop in $\bar{P}_{tot}$. While for the classical case (black lines in Fig. 4), after $t \approx 1L_y/c$, P_{tot} remains close to a factor of 30 above the initial state's $P_{tot,0}$, for higher B_0/B_Q in the more radiative cases (blue and red lines), the normalized power is limited and even decreases with time for the most radiative case. This is caused primarily by a decrease in the average particle kinetic energy due to radiative

cooling. As the cooling is particularly strong in the densest regions, where the magnetic field is compressed, the effect is enhanced by a loss of the positive correlation between the temperature and density found in the classical case discussed in Section 4.3.

In our previous work (Schoeffler et al. 2019), we showed that in 2D simulations radiative cooling led to significant additional compression of the magnetic field and density inside magnetic islands (most pronounced for the highest B_0/B_Q), caused by the necessity to maintain a magnetostatic equilibrium. The relatively weak guide field $B_G = 0.05 B_0$ adopted in that study was not able to prevent this compression, and this resulted in a concentration of much stronger radiative losses at the cores of the magnetic islands. One might then conjecture that this could lead to an enhanced overall normalized power in the more radiative cases, in an apparent contrast with our results presented here in Fig. 4(a). However, after performing a similar analysis to the data of that previous study, we find the results are qualitatively similar to those presented here. There was an initial sudden spike in $\bar{P}_{tot}$ once reconnection got started, but the enhancement was weaker for higher B_0/B_Q (more radiative cases) and it decayed with time [similar to Fig. 4(a)]. The localized enhancement of ϵ_{est} was not strong enough to counterbalance the overall cooling-driven decrease in $\bar{P}_{tot}$ for stronger B_0/B_Q. In fact, the decrease in relative power was even more pronounced than in the simulations of this work.

As shown in Fig. 4(a) [see also Fig. 4(c)] the estimated power $P_{tot,est}$ [see equation (17)], plotted with a dashed line in Fig. 4(a), is a qualitatively good predictor of P_{tot} and, in particular, qualitatively captures the dependence of $\bar{P}_{tot}$ on B_0/B_Q. In the classical case, $P_{tot,est}$ moderately underestimates P_{tot}, because it does not include the enhancement of radiation due to bulk flows and kinetic effects. For the intermediate case, it provides an excellent approximation. However, $P_{tot,est}$ overestimates P_{tot} somewhat for the radiative case. This overestimation is caused by kinetic effects that we will discuss in Section 4.4. As shown in Fig. 4(c), the ratio $P_{tot,est}/P_{tot}$ typically reaches as high as ~2 for the most radiative case.

The simpler normalized estimate of power $P_{tot,est2}/P_{tot,0}$ [see equation (18)] is shown as dashed lines in Fig. 4(b). During the active reconnection stage [$t \simeq (0.5 - 2)L_y/c$], it strongly underestimates the emitted power, by a factor as high as ~10; a significant underestimation, although not as dramatic, is observed at later times as well. The reason for this is that $P_{tot,est2}$ does not take into account the positive spatial correlation between strong magnetic field and large kinetic energy density (i.e. plasma pressure), which enhances the radiated power. This correlation will be discussed in more detail in Section 4.2 and Section 4.3. We highlight the importance of the correlation in Fig. 4(d) by taking the ratio of the estimated emission $P_{tot,est}$, which takes into account these correlations, to the estimation from $P_{tot,est2}$, which does not. This ratio can reach values as high as 7.

4.2 Spatial correlation between plasma density and the magnetic field

Compression of magnetic fields and density near the centres of magnetic islands leads to enhancements of the local emissivity $\epsilon(\mathbf{x})$, and the total emitted power P_{tot}. At about $t = 1L_y/c$, when the ratio $P_{tot,est}/P_{tot,est2}$, which quantifies the importance of the correlation, shown in Fig. 4(d), is highest, reaching a factor of about 5, the power in Figs 4(a) and (b) is significantly enhanced. During the next light-crossing time the enhancement drops down to about 3–4.

At the time $t = 1.5L_y/c$, the compression of n/n_b and B/B_0 is illustrated for both the classical case in Figs 5(a) and (b) and
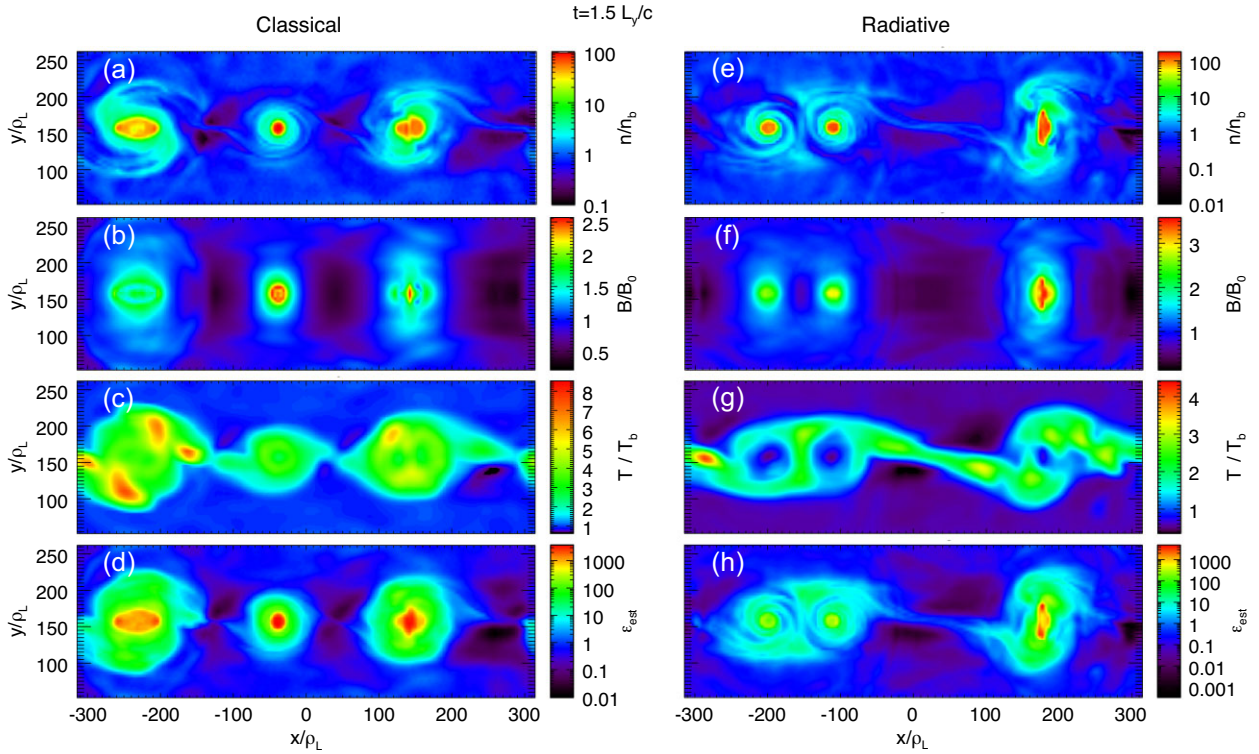
Figure 5. Left-hand column: Maps of (a) electron density, (b) total magnetic field, (c) effective temperature, and (d) normalized estimated local synchrotron emissivity $\epsilon_{\mathrm{est}}/\epsilon_{\mathrm{est},0} \sim nT^2B^2$ for the 2D classical case $B_0/B_Q = 4.5 \times 10^{-6}$ at $t = 1.5L_y/c$. Right-hand column: Respective maps (e,f,g,h) for the 2D radiative case $B_0/B_Q = 4.5 \times 10^{-3}$ at the same time $t = 1.5L_y/c$.

the radiative case in Figs 5(e) and (f). The corresponding plasma temperature maps are shown in panels (c) and (g) of Fig. 5 and will be discussed in more detail in Section 4.3. The maximum density and magnetic field are both found near the centres of the magnetic islands, indicating a clear correlation between the magnetic field energy and plasma densities.[1] We provide evidence of the enhancement of local emissivity by examining the estimated emissivity ϵ_{est} as a function of space in Figs 5(d) and (h), which shows the strongest emission exceeding the background levels by factors of more than 1000 in the centres of the magnetic islands.

In the radiative case, there is a noticeable decrease, throughout most of the volume, in the normalized $\epsilon_{\mathrm{est}}/\epsilon_{\mathrm{est},0}$ compared to the classical case [see Figs 5(d) and (h)], consistent with the drop in $P_{\mathrm{tot,est}}$ shown in Fig. 4(a). This can be explained by the reduction in the effective temperature caused by the radiative cooling. Interestingly, however, at the specific time $t = 1.5L_y/c$ shown in Fig. 5, the peak values of $\epsilon_{\mathrm{est}}/\epsilon_{\mathrm{est},0}$ for the radiative and the classical cases are about the same. This is because the negative effect of cooling on the emissivity is compensated, at this particular time, by the stronger peak compression of the magnetic field in plasmoid cores in the radiative case [see Figs 5(b) and (f)].

Indeed, in our previous paper (Schoeffler et al. 2019) we showed that the potential loss of pressure support inside the islands due to radiative cooling (most pronounced for the highest B_0/B_Q) is prevented by the enhanced compression of the plasma density, which

---

[1]Note that the apparent extremely strong (reaching $\gtrsim 100n_b$!) peak density enhancement inside island cores is mostly explained by the very high density of the plasma in the initial Harris layer, $n_0 = 37n_b$, which quickly collects in plasmoid cores and subsequently undergoes only a moderate compression.

in turn drives the compression of the magnetic field (see below). This compression, in principle, should lead to higher synchrotron emissivity. The compression is not as pronounced in the simulations presented here due to the stronger guide magnetic field $B_G/B_0 = 0.4$ instead of $B_G/B_0 = 0.05$ adopted in Schoeffler et al. (2019). However, it still counteracts the direct suppression of the emissivity by radiative cooling and hence may explain why the peak ϵ_{est} in Figs 5(d) and (h) was not strongly affected by the cooling.

The enhanced compression can be seen more clearly when examining the n-B histogram shown for the 2D simulations in Fig. 6 for $t = 3L_y/c$. However, before looking at the most compressed regions, let us examine the general features of this histogram. The basic expected feature, discussed in Section 3.2, is that most of the points start in the background at $n = n_b$, $B = \sqrt{B_0^2 + B_G^2}$, and follow the frozen-in scaling of equation (19). In the higher density region of the histogram, where $n/n_b > 1$, corresponding to the magnetic islands, a new scaling can be determined, also based on the flux-freezing law.

First, one should note that the plasma that was initially located deep inside the Harris current sheet, where $n = n_0 = 37n_b$, as was indicated by the blue X in Fig. 1 at $tc/L_y = 0.4$, has moved at later times to the centres of the magnetic islands. This population is represented by a very small number of very-high-density points in Fig. 6, extending up to $n/n_b \simeq 40$ in the classical case and up to $n/n_b \simeq 100$ in the radiative case. On the other hand, the new scaling under the discussion here corresponds to the outer parts of the magnetic islands containing newly reconnected magnetic flux and filled with background plasma, with density $n/n_b \gtrsim 1$.

Let us consider a moderately dense ($n \sim (2-5)\,n_b$), thin annular flux ribbon somewhere inside an island, encircling, but lying outside of, the island's dense, guide-field-dominated inner core. Let us
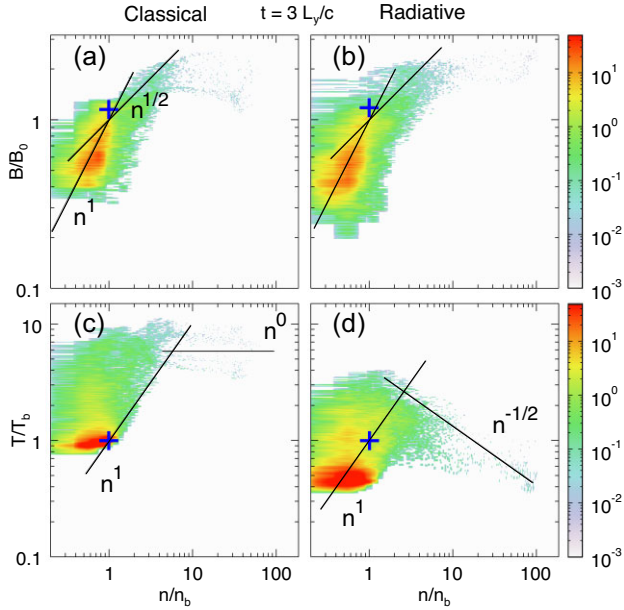
Figure 6. Top row: Histograms in *n-B* space at $t = 3L_y/c$ in terms of the local density n/n_b and magnetic field B/B_0, for (a) the 2D classical simulation and (b) the 2D radiative simulation. Bottom row: Similar histograms in *n-T* space in terms of the local density n/n_b and temperature T/T_b, for (c) the 2D classical simulation, (d) the 2D radiative simulation. The blue plus signs represent the initial conditions of the ambient background. The $B \sim n$ [equation (19)] and $B \sim n^{1/2}$ [equation (20)] scalings are shown with thin solid lines in the top panels. Similarly, the scalings $T \sim n$, $T \sim n^0$, and $T \sim n^{-1/2}$ are shown in the *n-T* space histograms in the bottom panels for reference.

examine the self-similar evolution of this ribbon, assuming that its radial thickness Δr and its radius r decrease in unison, in proportion to each other, as the island compresses over time, i.e. $\Delta r(t) \propto r(t)$. The number of particles $2\pi n r \Delta r$ and the in-plane magnetic flux $B_{xy}\Delta r$ enclosed within this flux ribbon should both be conserved as the radius shrinks (neglecting the decay of the magnetic flux due to radiative resistivity, see Appendices C and D). One can then obtain the following relationship, based on the characteristic values of n and B inside this flux ribbon, assuming that the in-plane magnetic field B_{xy} dominates over the guide field B_z, so that $B \simeq B_{xy}$:

$$\frac{B}{B_0} \sim \left(\frac{n}{n_b}\right)^{1/2}. \tag{20}$$

Strictly speaking, this relation should be followed only if the magnetic fields can be well described by a 2D model, since, in a real 3D situation, the compressed plasma could in principle escape the island in the out-of-plane direction.

We can see in the *n-B* histogram shown in Figs 6(a) and (b) that at $t = 3L_y/c$, the expected correlations (19) and (20) between n and B due to the frozen-in condition are followed for both the classical and radiative cases. For $n/n_b < 1$, it is clear that $B/B_0 \sim n/n_b$, while for $1 < n/n_b \lesssim 10$, $B/B_0 \sim (n/n_b)^{1/2}$ provides a good fit. For $n/n_b > 10$ (a few points outside of the bulk of the histogram, corresponding to the centres of the primary magnetic islands filled primarily with the initial dense current-sheet plasma), neither of the scalings equations (19)–(20) based on frozen-in flux hold, most likely because the compressed guide field B_z dominates here. However, we also observe a significant difference between the classical and radiative cases. For the classical case, the initial Harris sheet structure is retained; i.e. B decreases with n for very large densities. The initial current sheet was in pressure

balance, and thus the magnetic pressure initially decreased along gradients of increasing density. As plasma moves towards the high-density centres of the islands during reconnection, the histogram retains this trend [the magnetic field B/B_0 slightly decreases with n/n_b in regions of *n-B* space where $n/n_b > 10$, shown in Fig. 6(a)]. In contrast, the radiative cooling and subsequent compression present in the radiative case lead to a continued positive correlation between the magnetic field and the density, which results in a somewhat increased magnetic field compression in the radiative case [B/B_0 slightly increases with n/n_b above $n/n_b > 10$, shown in Fig. 6(b)].

4.3 Spatial correlation/anticorrelation between plasma temperature and density

While we briefly considered the importance of the correlation between the particle kinetic energy and the magnetic field energy in Section 4.1, we mostly focused on the correlation between the plasma density and magnetic field strength in Section 4.2 ignoring any dependence on temperature. The correlations of B and n with the temperature T are, however, important because the temperature strongly affects the local emissivity, $\epsilon \sim T^2$. In fact, in the classical case, there is a positive correlation between the temperature and compressing magnetic fields and density (albeit slightly less pronounced), leading to an even stronger enhancement of the local emissivity $\epsilon(\boldsymbol{x})$ and of P_{tot}. The enhanced temperature is caused both by heating and particle acceleration via reconnection and by the adiabatic compression of magnetic islands. One can see in Fig. 5(c) that the temperature is increased inside the islands, although it reaches its peak closer to the Y-point region where the reconnection outflows collide with the islands.

In contrast, in the radiative case, as seen in Fig. 5(g), there is a general reduction of temperature due to radiative cooling. In particular, the temperature becomes much lower at the centres of the islands, reaching a local minimum. This results in a negative correlation between n and T, which, along with the general cooling, helps explain the clear reduction in $\bar{P}_{\text{tot}}$ shown in Fig. 4(a) for the more radiative cases.

These correlations are also clearly visible in the *n-T* histograms. In the classical case shown in Fig. 6(c), there is a clear positive correlation between n and T, particularly visible on the right (high-n) border of the histogram (with a scaling around $T \sim n$), while the temperatures in the highly compressed ($n \gtrsim 5n_b$) regions, including island cores, seem to be weakly dependent on n. However, in the radiative case Fig. 6(d), one observes an inverse correlation between n and T when these reach their maximum values (with a scaling around $T \sim n^{-1/2}$). This is expected due to the enhanced cooling at higher B which corresponds to higher densities [as seen in Fig. 6(b)].

4.4 Kinetic effects

The estimate $P_{\text{tot, est}}$ is based on fluid quantities, assuming that an isotropic Maxwell-Jüttner distribution in the given species' comoving frame is maintained and thus ignores kinetic effects. However, the particle momentum distribution does not in fact remain Maxwellian or isotropic, and the average particle energy alone no longer suffices to determine the emissivity. Radiation is dominated by more energetic particles and particles with velocities making large angles with respect to the magnetic field; it is thus affected by features like, respectively, super-Gaussian energy distributions and anisotropic pitch-angle distributions. Pitch-angle distribution anisotropy, e.g. caused by the predominant synchrotron cooling of high pitch-angle particles, reduces the emission relative to the level
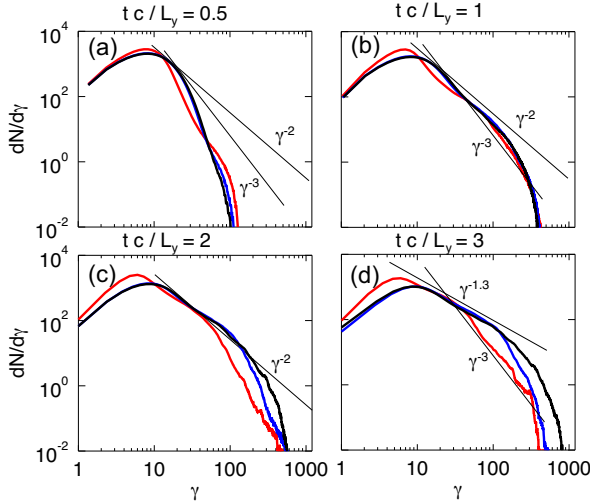
Figure 7. Electron energy distributions for the 2D classical case $B_0/B_Q = 4.5 \times 10^{-6}$ (black), the intermediate case $B_0/B_Q = 4.5 \times 10^{-4}$ (blue), and the radiative case $B_0/B_Q = 4.5 \times 10^{-3}$ (red), at $tc/L_y =$ (a) 0.5, (b) 1, (c) 2, and (d) 3.

predicted by $P_{\rm tot, est}$, which may explain the increase in the ratio $P_{\rm tot, est}/P_{\rm tot}$ seen in Fig. 4(c) for the more radiative simulations. On the other hand, non-thermal high-energy particles accelerated during reconnection, which do not always provide a significant contribution to the effective temperature and hence to $P_{\rm tot, est}$, are expected to radiate significantly more, making $P_{\rm tot, est}$ an underestimate; this may explain the drop in $P_{\rm tot, est}/P_{\rm tot}$ occurring at the onset of magnetic reconnection around $tc/L_y \approx 0.5$, also visible in Fig. 4(c) for all three cases.

The energy distributions of the background electrons, shown in Fig. 7 at several different times, display the formation of a non-thermal population after $t = 0.5L_y/c$ [Fig. 7(a)]. By $t = 3L_y/c$ [shown in Fig. 7(d)], the distribution for the non-radiative case (black) evolves to a hard power law with an index $\alpha \approx 1.3$, whereas in the radiative case (red) there is a spectral break to a steeper high-energy power law with an index $\alpha \gtrsim 3$, consistent with previous results by Werner et al. (2016, 2018b); Hakobyan et al. (2019).

The moments of the distribution, $<\gamma>$ (temperature), and $<\gamma^2>$ (power radiated), can help us understand the drop in $P_{\rm tot, est}/P_{\rm tot}$ seen in Fig. 4(c) starting at $t \sim 0.5L_y/c$. This drop corresponds to situations where the power-law index of the non-thermal part of the particle energy distribution falls between 2 and 3. Indeed, such a power law has a peculiar property that the first moment of the distribution function (and hence the effective temperature) is dominated by the lower energy particles with γ near the peak of the distribution, while the second moment (and hence the radiated power) is dominated by the highest energy particles. That is, different particle sub-populations are responsible for the temperature, which enters into $P_{\rm tot, est}$, and for the actual emissivity, which enters into the directly measured $P_{\rm tot}$; this leads to an underestimation of the emitted power by $P_{\rm tot, est}$. We can see in Fig. 7(b) that at $t \sim 1L_y/c$ the developing power law has become hard enough so that its spectral index is between the critical values 2 and 3 (for the classical and intermediate cases), and this corresponds to a dip in the $P_{\rm tot, est}/P_{\rm tot}$ ratio in Fig. 4(c). By $t \sim 2L_y/c$ [see Fig. 7(c)], however, the non-thermal spectra in the classical and intermediate cases, as well as the moderate-energy uncooled part of the spectrum in the radiative case, have hardened even further and their power-law indices start to drop below 2. Both the temperature (the first moment) and the

radiative emissivity (the second moment) are now dominated by the same, highest energy, particle populations and hence (ignoring the effects of radiative cooling on the pitch-angle distribution which allow $P_{\rm tot, est}/P_{\rm tot}$ to exceed unity in the radiative case) $P_{\rm tot, est}$ becomes a better estimation of the emitted power.

Kinetic effects are therefore expected to enhance the radiated power compared to the average-energy-based estimations ($P_{\rm tot} > P_{\rm tot, est}$) during the early stages of magnetic reconnection, and diminish it ($P_{\rm tot} < P_{\rm tot, est}$) as time progresses for more strongly radiative systems.

In summary, in this section, we have shown that, in 2D relativistic radiative reconnection, the total radiated power $P_{\rm tot}$ is increased at the onset of magnetic reconnection due to the heating and acceleration of particles in the plasma by reconnection, enhanced by the compression and correlation of magnetic fields and plasma density at the centres of magnetic islands, which can be reasonably well captured by $P_{\rm tot, est}$, but not by $P_{\rm tot, est2}$. In addition, the kinetic, non-thermal effects, which are ignored by $P_{\rm tot, est}$, can further enhance the radiated power at these early times. However, we have also shown that, in the most radiative cases, radiative cooling leads to a pronounced anticorrelation of temperature with density and magnetic field; this causes a decrease in the normalized radiated power $\bar{P}_{\rm tot}$. As a result, at late times the enhancements in radiation can be cancelled out, and both $P_{\rm tot, est}$ and $P_{\rm tot, est2}$ become better predictors.

5 3D RESULTS

As in the 2D study of Section 4, in this section we will explore results from three simulations using the fiducial parameters from Section 2 ($\sigma_h = 25.76$, $B_g/B_0 = 0.4$, $L_x/\rho_L = L_y/\rho_L = 314.4$, etc.) with varying levels of radiation strength: the classical case $B_0/B_Q = 4.53 \times 10^{-6}$, the intermediate case $B_0/B_Q = 4.53 \times 10^{-4}$, and the radiative case $B_0/B_Q = 4.53 \times 10^{-3}$. In these 3D simulations, we adopt the system size in the third dimension to be $L_z/\rho_L = 58.6$ ($L_z/L_y = 0.19$). Although this value of L_z is rather small, given our guide field $B_G/B_0 = 0.4$, it still allows the system to exhibit important dynamics in the $\hat{z}$ direction including the development of a kinking instability. We did conduct a parameter-space study varying the guide field in Section 6.1 and L_z in Section 6.2 to justify this choice. We again show the process of reconnection, the effects that radiation has on it, and now how 3D results differ from 2D. As we will show below, while the guide field keeps the dynamics similar to the 2D case, and many of the standard predictions of reconnection do not differ strongly, the development of a kink mode significantly limits the density compression compared to that found in 2D.

Again, in all cases, the initial current sheet is unstable to the tearing instability, and multiple magnetic islands (plasmoids; flux ropes in 3D) form, driven by magnetic reconnection that converts the upstream magnetic energy into the particle kinetic energy in the form of bulk outflows, heating, and non-thermal particle acceleration. The plasma density map in the current sheet, with superimposed magnetic field lines, shown in Fig. 8, illustrates the generation and merging of 3D plasmoids during the first light crossing time in the radiative case. Like in 2D, these dynamics are representative and similar to the other two cases.

The conversion of energy from the magnetic fields to the kinetic energy of the plasma particles (both heating and bulk flows) as a function of time is shown for the three cases in Fig. 9, comparing the 3D simulations to the 2D ones. Like in 2D, the particle kinetic energy is rapidly converted into radiation for the more radiative cases, where the radiated energy fraction increases with the strength of radiative cooling characterized by B_0/B_Q. The onset of reconnection,
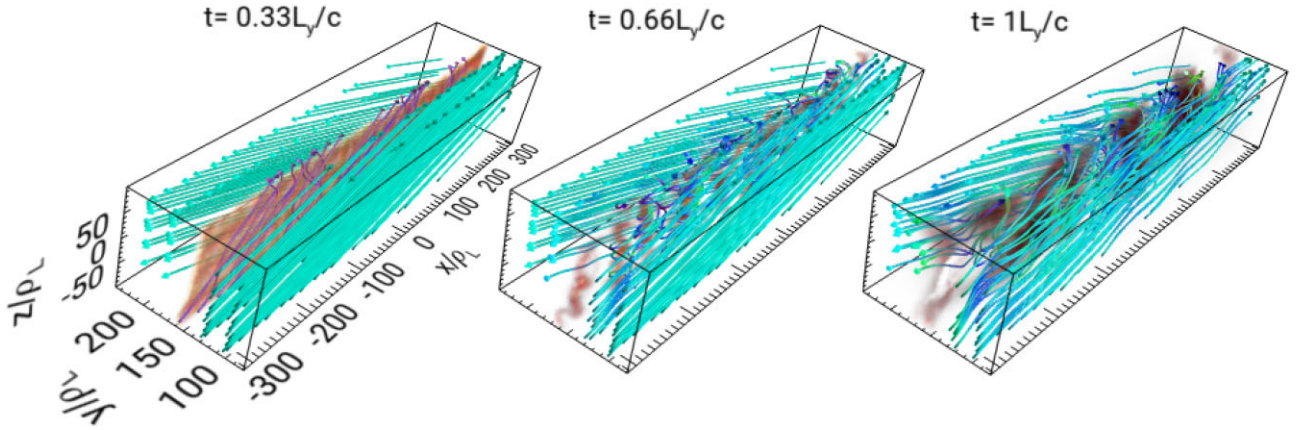
Figure 8. Zoom-in on the upper current sheet, showing magnetic field lines (green) and a volume rendering of the plasma density (brown), for the 3D radiative case $B_0/B_Q = 4.5 \times 10^{-3}$, at (a) $t = 0.33L_y/c$, (b) $t = 0.66L_y/c$, and (c) $t = 1L_y/c$.
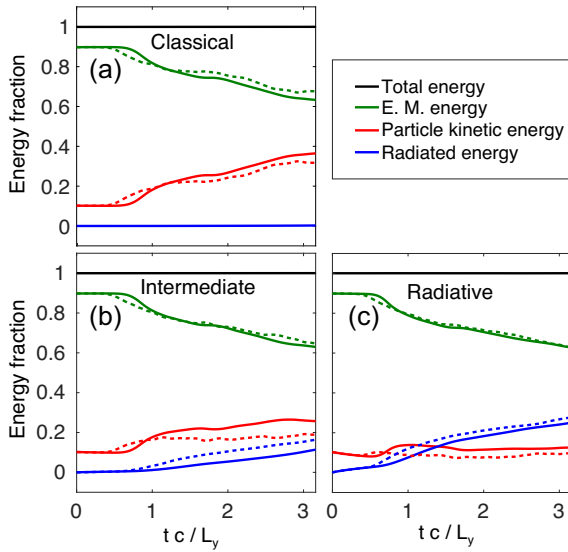
Figure 9. Time-evolution plots of energy partition between electromagnetic (green), particle kinetic (red), and radiated (blue) energies, along with their sum (black), for the 3D simulations with (a) $B_0/B_Q = 4.5 \times 10^{-6}$, (b) $B_0/B_Q = 4.5 \times 10^{-4}$, and (c) $B_0/B_Q = 4.5 \times 10^{-3}$. For reference, the dotted lines represent the same quantities for the 2D cases.

and thus energy transformations occur somewhat later in 3D, but the decay in magnetic energy eventually follows similar curves. Furthermore, for the 3D intermediate and radiative cases, there is slightly less radiation and therefore more particle kinetic energy at late times.

Again we calculate the reconnection rate by looking at the difference in magnetic flux between the two current sheets (using two measures, the difference between the average flux along the planes of the initial current sheets $y = \pm L_y/2$, and between the maximum and minimum values in each of these planes). Although in 3D a magnetic flux function is difficult to define in a unique way, we estimate one after averaging the magnetic fields along $\hat{z}$. The rate at which the flux decreases, for the radiative case, gives us a normalized reconnection rate of 0.04 and $0.125B_0c_A$ using the two respective measures of flux, a factor of 2 slower than the equivalent measures in 2D; however, this rate persists for the whole duration of the simulation in agreement with Werner & Uzdensky (2021). Also, as in 2D, we do not find a

significant dependence of the reconnection rate on radiative cooling strength.

5.1 Comparisons of radiation, field maps, and their correlations between 3D and 2D simulations

For the most part, the power emitted (including its spectra) and its estimates based on the spatial distributions of density, magnetic field, and temperature from the 3D simulations are qualitatively the same as in 2D. Generally, diagnostics differ only by factors of about 2, and we will note some of these modest differences. However, we will highlight one significant difference: 3D effects tend to disrupt the dense concentrated regions with significantly higher local emissivity at the centres of plasmoids that were found in 2D.

First, the total power and its estimates are qualitatively similar in 2D and 3D. This can be seen in Figs 10(a) and (b), where the actual emitted power P_{tot} and its estimates $P_{\text{tot, est}}$ and $P_{\text{tot, est2}}$ are roughly comparable to those shown in Figs 4(a) and (b) (the dotted line in Fig. 10 shows the 2D classical result for reference). However, there are still substantial quantitative differences. The emitted power grows more slowly in 3D, although eventually it reaches magnitudes that are fairly similar to (but slightly less than) those found in 2D. The normalized emitted power $\bar{P}_{\text{tot}}$ begins to increase at $t = 0.6 - 0.7L_y/c$, about a factor of 1.3 later than in 2D. In addition, whereas in the 2D non-radiative case $\bar{P}_{\text{tot}}$ stays nearly flat for $t \gtrsim 1L_y/c$, in 3D it undergoes a steady rise after about $t \simeq 2L_y/c$, so that the total 2D and 3D radiative powers become very close at late times. The 3D radiative case differs substantially from its 2D counterpart in terms of the time behaviour of $P_{\text{tot, est}}/P_{\text{tot}}$. In 2D, this ratio [the red curve in Fig. 4(c), also shown in Fig. 10(c) as the dotted red curve] quickly rises and then saturates at a level corresponding to $P_{\text{tot, est}}$ overestimating P_{tot} by a factor of about 2. For the 3D case, shown in Fig. 10(c) with a solid red line, the ratio $P_{\text{tot, est}}/P_{\text{tot}}$ grows slowly with time throughout the whole simulation, so that $P_{\text{tot, est}}$ underestimates P_{tot} until about $tc/L_y = 2$ and reaches the levels of overestimation comparable to the 2D case only by $tc/L_y = 3$. Like in 2D, energy is predominantly radiated by the high-energy electrons and positrons moving roughly perpendicular to the magnetic field, leading to deviations from a Maxwellian distribution. Unlike in 2D, the time evolution of these deviations spans the full duration of the simulation.

The enhancement of radiation due to the correlation between the magnetic $B^2/8\pi$ and thermal nT energies is similarly present in 2D and 3D. In Section 4.1 we showed that the importance of
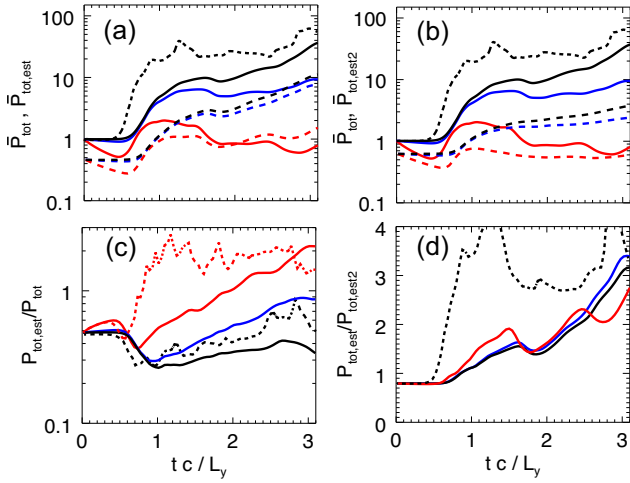
Figure 10. (a) Total normalized radiated power $\bar{P}_{tot} \equiv P_{tot}/P_{tot,0}$ (solid lines) for 3D simulations with $B_0/B_Q = 4.5 \times 10^{-6}$ (black, classical case), 4.5×10^{-4} (blue, intermediate case) and 4.5×10^{-3} (red, radiative case). These colours are used for all panels in this figure. For reference, the black dotted lines represent the same quantities as the solid lines but for the 2D classical case (radiative case shown in red in panel c). The dashed lines represent the normalized estimated power $\bar{P}_{tot,est} \sim \langle nT^2B^2 \rangle$ [see equation (17)]. (b) Total normalized radiated power $\bar{P}_{tot}$ (solid lines) and the second normalized power estimation $\bar{P}_{tot,est2} \sim \langle nT \rangle^2 \langle B^2 \rangle$ [see equation (18)] in dashed lines. (c) Ratio $P_{tot,est}/P_{tot}$. (d) Ratio of the two estimations of power radiated $P_{tot,est}/P_{tot,est2}$.

this correlation can be quantified by the ratio $P_{tot,est}/P_{tot,est2}$, shown in Fig. 4(d). In 2D this ratio, shown with a dotted black line for the non-radiative case, rises rapidly during the onset of magnetic reconnection and reaches a saturated value. This differs in 3D [see Fig. 10(d)], where the ratio $P_{tot,est}/P_{tot,est2}$, continues to grow slowly and steadily without reaching saturation, and consequently so does the normalized emitted power $\bar{P}_{tot}$ [in Figs 10(a) and (b)] (except for the radiative case, where radiative cooling causes a decrease in the normalized power).

The most notable difference between the 3D and 2D simulations is that there is significantly less compression of the density in 3D. The respective enhancements of density, shown in Figs 11(a) and (e), and of the magnetic field, shown in Figs 11(b) and (f), reach values of $\sim20n_b$ and $\sim(1.5-2)B_0$, compared to the $\sim100n_b$ or $\sim3B_0$ in the 2D case. The density concentration is thus almost an order of magnitude weaker in 3D, while the enhancements of the magnetic field and the temperature, shown in Figs 11(c) and (g), are only about a factor of 2 smaller. Similar to the 2D case shown in Fig. 5, the spatial correlations between the peak density, magnetic field, and, for the classical case, temperature in Fig. 11, are visible.

All else being equal, the weaker density compression leads to significantly weaker emissivity at the centres of plasmoids in 3D. The estimated local emissivity ϵ_{est} reaches peak values that are significantly lower (by a factor of about 10) in 3D than in 2D. This means that in 3D, regions with significant radiation emission are less concentrated and are spread over a larger volume. Note that, despite this strong difference in the peak ϵ_{est}, the total emitted power P_{tot} remains roughly the same in both 2D and 3D simulations (only a factor of about 2 higher in 2D).

The limit on the density compression can be seen in the *n-B* histogram shown in Fig. 12. Like in 2D, in 3D the correlations between *n* and *B* due to the frozen-in condition are followed according to equation (19) for $n/n_b < 1$. However, in 3D, as magnetic

tension squeezes the plasma to a higher density in a magnetic island, the plasma is free to move out along the $\hat{z}$ direction to regions with a weaker magnetic field. Therefore, variations along the $\hat{z}$ direction caused by, for example, the kink instability, prevent the *n-B* distribution from following equation (20) for $n/n_b > 1$ as found in 2D. Furthermore, compression of the density is also limited, and the maximum n/n_b drops from ~100 to close to 30 (i.e. less than the initial current-sheet density $n_0/n_b = 37$). Not only is the density enhancement limited, but the plasma is also allowed to spread broadly across *n-B* space, eventually revealing power-law limits that will be described further in Section 5.2.

In 3D, the plasma is not as easily trapped and compressed at the centres of plasmoids, where it can be strongly cooled, as occurs in 2D. Therefore, the anticorrelation between the magnetic field (density) and the temperature, found in the radiative case, is not as strongly pronounced in 3D. This can be seen by comparing Figs 11 and 5. However, the cooling still leads to an anticorrelation in 3D.

The similarity of these (anti)correlations between 2D and 3D cases can be also noted from the *n-T* histograms. In the classical case shown in Fig. 12(c), there remains a clear positive correlation between *n* and *T*, roughly consistent with the relativistic adiabatic scaling $T \sim n^{1/3}$, for the whole range of *n*. In contrast, in the radiative case, see Fig. 12(d), an inverse correlation between *n* and *T* is visible near the maximum values, with a power-law slope close to $n^{-1/2}$.

Finally, the particle energy spectra are almost the same in 3D as in 2D, in agreement with previous studies (Werner & Uzdensky 2017). In 3D, shown in Fig. 13, the non-thermal electron population in the particle energy distribution forms more slowly than in the 2D case (shown in Fig. 7), and is not yet present by $t = 0.5L_y/c$. However, similar to 2D, at late times ($tc/L_y = 2 - 3$) a power-law tail is fully formed in 3D runs, with the index reaching $\alpha \approx 1.3$ for the radiative case (at moderate energies) and ≈ 1.5 for the other cases. Once again, in the 3D radiative case, there is a spectral break to a steeper power law with $\alpha \gtrsim 3$ at higher energies. These results remain consistent with the results of 2D radiative reconnection PIC simulation studies by Werner et al. (2018b) and Hakobyan et al. (2019). The limit on the maximum energy of the most energetic electrons is stricter in 3D than in 2D. As in 2D, kinetic effects influence the accuracy of the estimated power. The spectral index $2 < \alpha < 3$ occurs between $t = (1 - 2)L_y/c$ and may help explain the underestimation of P_{est}, particularly in the classical case, in Fig. 10(c).

We should also remark that, based on the radiative case's background magnetic field strength of $B_0/B_Q = 4.53 \times 10^{-3}$, all particles with Lorentz factors $\gamma \gtrsim 15$ are expected to emit synchrotron radiation in the gamma-ray regime (i.e. with $\hbar\omega > m_ec^2$), thus potentially feeding powerful pair creation. While for simplicity we have excluded pair-production effects and other QED physics from this study, incorporating them self-consistently in PIC studies and examining their back-reaction on the reconnection process itself constitutes a particularly interesting and exciting frontier of extreme plasma astrophysics (Uzdensky 2011; Beloborodov 2017; Hakobyan et al. 2019; Schoeffler et al. 2019; Mehlhaff et al. 2021; Chen et al. 2023; Hakobyan et al. 2023b).

5.2 Histogram boundaries in 3D

As mentioned in Section 3.2, one of the most striking features of the histogram diagnostic from the 3D simulations is that the local levels of magnetic field and density compression are bounded by clear and distinct power laws in the *n-B* space. The late-time ($t = 3L_y/c$) histograms for both the classical and radiative cases are shown in Fig. 12. One can see at the top of the histogram for both these cases,
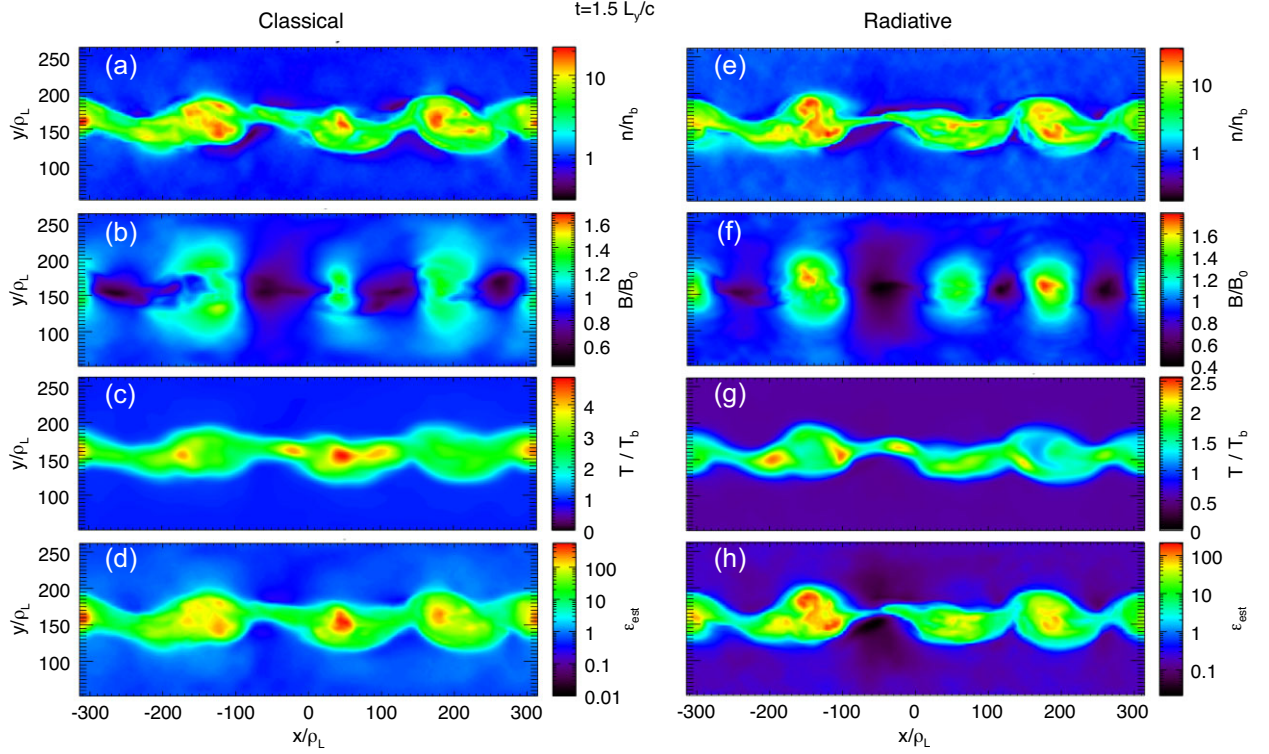
Figure 11. Left-hand column: Maps of (a) electron density, (b) total magnetic field, (c) effective temperature, and (d) normalized estimated local synchrotron emissivity $\epsilon_{est}/\epsilon_{est,\,0} \sim nT^2B^2$ at a representative slice $z = -4/5\,L_z$ for the 3D classical case $B_0/B_Q = 4.5 \times 10^{-6}$ at $t = 1.5L_y/c$. Right-hand column: Respective maps (e,f,g,h) for the 2D radiative case $B_0/B_Q = 4.5 \times 10^{-3}$ at the same time $t = 1.5L_y/c$.

in Figs 12(a) and (b), an upper bound on B given by the power law $B/B_0 \sim (n/n_b)^{1/12}$. At the top of the histogram of the radiative case, in Fig. 12(b), an additional upper bound on B, given by the power law $B/B_0 \sim (n/n_b)^{1/6}$, is seen at lower densities. Also, to the right of the histogram for both cases, in Figs 12(a) and (b), an upper bound on n can be described as $B/B_0 \sim (n/n_b)^1$. It is also worth mentioning that there is a very clear, robust lower boundary of this histogram: $B_{min} \simeq 0.3B_0$, essentially independent of n.

To put this in context, the best-fitting lines of the boundaries over the entire ranges of n and B for the 3D radiative case presented in Fig. 1(d) correspond to $B/B_0 = 1.5(n/n_b)^{0.11}$ and $B/B_0 = 0.23(n/n_b)^{2/3}$. The $0.11 \simeq 1/9$ slope of the best-fitting upper boundary appears to be roughly an average between the 1/6 and 1/12 slopes; it is an artefact of fitting with a single power law a function that is better described as a broken power law. Likewise, the discrepancy between the slopes of the right boundaries shown in Fig. 1(d) and Fig. 12(b) occurs because, at $tc/L_y = 3$, the power-law boundary is also not distinct along the full range in n-B space. The right boundary does not fit a single power law for low values of magnetic field ($B/B_0 \lesssim 0.6$), and therefore the automatic fit, when applied to the entire range of magnetic-field variation, $B/B_0 \simeq 0.3 - 2$, does not give an accurate measure of the slope of this power-law boundary. However, the fit still provides a good measure of the maximum compression of both B and n via the intersection point between the two limiting lines, indicated by red plus signs in Fig. 12.

Below we describe a couple of theoretical models that may be used to explain these power laws, and to get an order-of-magnitude estimate of the coefficients in front, allowing us to determine the maximum compression theoretically.

5.2.1 Density boundary

To the right of the histogram in Figs 12(a) and (b) there is a power-law boundary limiting the compression of the plasma density. In Appendix B, we present a possible explanation for a boundary with a slope $B_{min} \sim n$ [see equation (B1)], based on the marginal condition for the onset of the kink instabilities found in 3D. Initially, the current sheet can become unstable to the relativistic drift-kink instability (RDKI), while later, the current filaments (flux ropes) can be unstable to other modes including MHD kink. The kinking of the current filaments, which constitute the highest density regions, allows the plasma to escape to new locations, thereby checking the growth of the density due to compression. Regions to the right of this histogram boundary are subject to instability, while regions to the left are stable.

Fig. 14(a) shows that this compression boundary in fact occurs where the electric current density is highest. Instead of the distribution density of the histogram, the average normalized current density j/j_0 is shown here for each location in the n-B space. The normalization $j_0 \equiv en_0c$ is about equal to the initial peak current density $1.08j_0$. The highest current densities are located at the upper part of the right boundary in the n-B space given by equation (B1) in Appendix B, suggesting that the location of the boundary is determined by the unstable kinking of current filaments.

The formation of the boundary can be observed as the kink instability evolves. Initially, the centre of the current sheet, marked by an X in Fig. 1(a), is unstable to the RDKI. After 1 light crossing time, as seen in Fig. 1(b), the plasma evolves, pushing the histogram into new regions of the n-B space where n tends to be smaller; while lower densities (often with lower current densities) decrease the likelihood of kink instabilities, some of these regions can still be
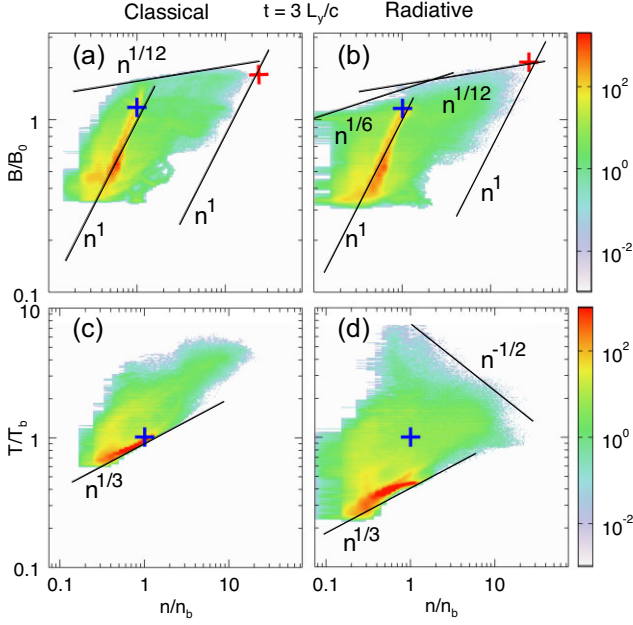
Figure 12. Top row: Histograms in *n-B* space at $t = 3L_y/c$ in terms of the local density n/n_b and magnetic field B/B_0 for (a) the 3D classical case and (b) the 3D radiative case [same as in Fig. 1(d)]. Bottom row: Similar histograms in *n-T* space in terms of the local density n/n_b and temperature T/T_b, for (c) the 3D classical case, (d) the 3D radiative case. The blue plus signs represent the initial conditions of the ambient background, while the red plus signs in the *n-B* histograms mark the upper right vertex of the best-fitting polygon boundary of the histogram, as explained in Section 3.2; the *n-B* coordinates of this vertex are plotted versus time in Fig. 15. The scalings $B \sim n$ [equation (19) and equation (B1)], $B \sim n^{1/6}$ [equation (D7)], and $B \sim n^{1/12}$ are shown with thin solid black lines in the top panels, while the $T \sim n^{1/3}$ and $T \sim n^{-1/2}$ scalings are shown in the *n-T* space histograms in the bottom panels for reference.
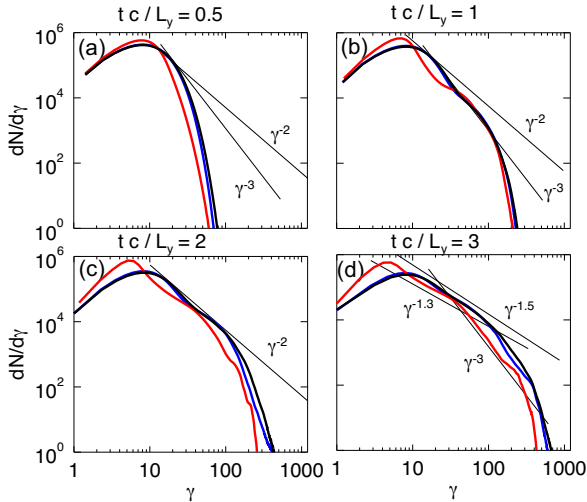
Figure 13. Electron energy distributions for the 3D classical case $B_0/B_Q = 4.5 \times 10^{-6}$ (black), the intermediate case $B_0/B_Q = 4.5 \times 10^{-4}$ (blue), and the radiative case $B_0/B_Q = 4.5 \times 10^{-3}$ (red), at $tc/L_y = $ (a) 0.5, (b) 1, (c) 2, and (d) 3.
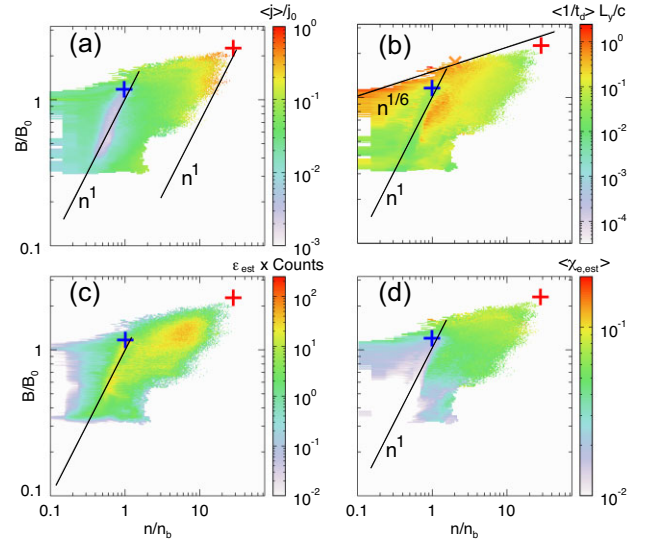
Figure 14. 2D maps in *n-B* space of the local average (a) current density $<j> /j_0$, (b) radiative-resistive magnetic dissipation rate $<1/t_d> L_y/c$ from equation (D3), (c) histogram distribution weighted by the local estimated emissivity ϵ_{est} from equation (16), and (d) $<\chi_{e, est}>$ based on equation (9) with $\gamma = 2\Theta_e$, at $t = 3L_y/c$ for the 3D radiative case. The blue plus signs represent the initial conditions of the ambient background, the red plus signs represent the upper right vertex of the best-fitting polygon boundary (see Section 3.2), which is plotted versus time in Fig. 15. The $B \sim n$ [equation (19) and equation (B1)] and $B \sim n^{1/6}$ [equation (D7)] scalings are shown with thin solid lines. The orange cross in panel (b) represents the intercept of the $n^{1/6}$ upper boundary assuming $L_y/ct_d = 0.7$, as explained in the text.

unstable, and kink instabilities continue to grow. After 2 or 3 light crossing times, the non-linear development of the kink instability is expected to mix high and low-density regions, eventually leaving only regions (confined by a boundary in *n-B* space) where we predict the kink instabilities to be stable.

In Appendix B, the $B \sim n$ boundary is predicted to occur where $(B/B_b)/(n/n_B) \approx 0.08$ [see equation (B10)]. We test our hypothesis by considering the boundary region, using the local maximum values of compressed islands, $B/B_0 = 2.2$ and $n/n_b = 28.8$, from the intersection in Fig. 1 (indicated by red crosses in Figs 12 and 14), matching the theoretical predictions remarkably well.

5.2.2 *Magnetic-field boundary*

Above the histogram in Fig. 12, there are power-law boundaries that limit the magnetic field compression. There is an empirically determined boundary with the scaling $B \sim n^{1/12}$, found in both classical and radiative cases. However, there is also evidence for another, somewhat steeper slope, $B \sim n^{1/6}$, for the radiative case at low and moderate plasma densities. Its origin is elucidated in Appendix D [see equation (D7)] based on the radiative dissipation of the magnetic flux, associated with an effective synchrotron resistivity

$$\eta_{\mathrm{eff}} \simeq \frac{40}{9} \frac{e^2 B^2}{n m_e^2 c^5} \left(\frac{T}{m_e c^2} \right)^2, \tag{21}$$

a function of the local values of *n*, *B*, and *T*, derived in Appendix C [see equation (C10)]. Therefore, in the radiative case, the combination of this slope and the shallower power law $B \sim n^{1/12}$ exhibited in the higher density segment of the boundary (see Fig. 12) effectively

leads to the intermediate best-fitting power law $\alpha = 0.11$ over the whole range of n, plotted in Fig. 1(d).

In the interest of understanding the 1/6 slope, we look at the 3D radiative case in Fig. 11(h), which shows the emissivity map at $t = 3L_y/c$. It is evident that most of the radiation is produced near the centres of plasmoids where the magnetic field is strongest (the local estimated emissivity ϵ_{est} is greatest there). As shown in Appendix D, the magnetic field dissipation rate via effective radiative resistivity in plasmoid cores is proportional to B^2T^2/n. Given the parameters of the 3D radiative simulation (described in Appendix D), the corresponding magnetic dissipation time-scale t_d is comparable to the radiative cooling time t_c. Therefore, it is expected that the radiative dissipation has sufficient time to occur and to dominate in these hot, strongly magnetized regions.

To provide firmer evidence that radiative dissipation is most relevant near the upper boundary in n-B space, in Fig. 14(b), instead of the distribution of the histogram, we show the average value of the normalized magnetic dissipation rate $<1/t_d > L_y/c$ [see equation (D3) from Appendix D] for each location in n-B space. Although we argued earlier that the radiative dissipation is most relevant in regions where the emissivity ϵ_{est} is greatest, $<1/t_d > L_y/c$ better determines the relevant regions. The picture is, therefore, somewhat nuanced and we need to distinguish two classes of plasmoids. First, the cores of primary, first-generation, plasmoids, filled mostly with the dense plasma from the initial Harris current sheet, have the highest emissivity ϵ_{est}; however, their radiative-resistive magnetic decay rate $t_d^{-1} \propto B^2T^2/n$ is relatively low because of its inverse scaling with density and because of the cooling-induced anticorrelation between temperature and density. In contrast, the low-density (and hence relatively low-emissivity) cores of secondary plasmoids, filled with the more tenuous upstream background plasma, have much higher $<1/t_d > L_y/c$; this is basically because, in order for a smaller number of particles to carry a sufficient current, they must move faster. As one can see in Fig. 14(b), the largest values of $<1/t_d > L_y/c$ are indeed found at the lower density ($n \lesssim 2n_b$) part of the upper power-law boundary in n-B space. This is clear evidence that the $B \sim n^{1/6}$ limit on the strength of the magnetic field is indeed related to radiative dissipation.

One can further verify the model by estimating the location of the boundary in n-B space, i.e. the normalization of the power-law scaling. One can estimate the limit of B/B_0 at $n/n_b = 2$, near the end of the $n^{1/6}$ scaling, by solving the expression for L_y/ct_d from Appendix D [see equation (D3)] with respect to B/B_0, imposing the requirement of significant dissipation during a crossing time, e.g. $L_y/ct_d \approx 0.7$ (a reasonable number chosen to fit the boundary). By taking the parameters of the radiative simulation: $B_0/B_Q = 4.53 \times 10^{-3}$, $L_y/\rho_L = 314$, and $\sigma_h = 25.76$, taking the characteristic filament radius from Fig. 11 to be $r/\rho_L = 20$, and setting $\theta_{e, loc} \approx 5(n/n_b)^{1/3}$, one obtains $B/B_0 \approx 1.7$. This is in reasonable agreement with the limits on the histogram shown in Fig. 14(b), where this point is highlighted with an orange cross. The $B \sim n^{1/6}$ scaling in Fig. 12(b) is valid only for low density $n/n_b \leq 2$, and is then replaced by a shallower scaling $B \sim n^{1/12}$ at higher densities. In principle, for more radiative systems, this scaling would be valid for the full range of densities.

5.2.3 Plasmoids and their compression

While discussing the limits on compression, we have focused our attention on the most significant source of radiation, the compressed regions inside plasmoids. Despite the small area they occupy, the total power they radiate may exceed that from the entire upstream region.
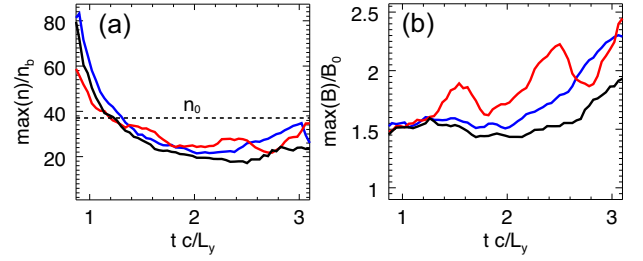
Figure 15. Peak (a) density and (b) magnetic field corresponding to the upper right vertex of the best-fitting polygon boundary of the n-B histogram (see Section 3.2), indicated in Figs 12 and 14, as functions of time for 3D simulations with a range of magnetic field strengths: $B_0/B_Q = 4.5 \times 10^{-6}$ (black, classical case), 4.5×10^{-4} (blue, intermediate case), and 4.5×10^{-3} (red, radiative case). The dotted line in panel (a) is the initial density at the centre of the Harris current layer.

In Fig. 14(c), the distribution in n-B space is weighted by the value of ϵ_{est} for each grid point. This figure illustrates both the significant power radiated from the upstream region, where $B \simeq (B_0^2 + B_G^2)^{1/2}$ and $n \simeq n_b$, and the even greater power radiated from the compressed plasmoid cores, centred around $B = 1.3B_0$ and $n = 6.5n_b$. Most of these plasmoid regions are located in between (and far from) the two boundaries in n-B space, where neither the density and current are so high that kinking plays a role, nor are the magnetic field and hence $<1/t_d > L_y/c$ so large that radiative dissipation becomes important. Thus, the compact, compressed plasmoid-core regions become brightly shining fireballs that contribute significantly to, and perhaps even dominate, the overall emission.

We also wish to highlight the trend that the estimated $\chi_{e,est} \equiv (2T/m_ec^2) B/B_Q$ increases in regions of stronger compression (higher B/B_0), as seen in Fig. 14(d). We, therefore, expect that for systems with stronger compression, and hence stronger B, $\chi_{e, est}$ could approach or exceed unity, leading to significant discrete hard gamma-ray emission and pair production.

In 3D, it is possible to define a useful and simple measure for quantifying the compression of plasmoids using the power-law boundary fits described in Section 3.2. For times $t > L_y/c$, i.e. after the clear boundaries have developed, a useful measurement of the maximal degree of compression is given by the intersection of the two boundaries in n-B space at the upper right vertex of the histograms. This intersection is indicated by the red ' + ' signs at $t = 3L_y/c$ for the classical case in Fig. 12(a), where $(n/n_b, B/B_0) = (24.0, 1.86)$, and for the radiative case in Fig. 12(b), where $(n/n_b, B/B_0) = (28.8, 2.18)$. We present this measurement of compression for both n in Fig. 15(a) and B in Fig. 15(b) as functions of time. Unfortunately, this diagnostic does not work well for the histograms based on our 2D simulations, and thus we only present this diagnostic in 3D.

Although this diagnostic is not yet available before $t \sim 1L_y/c$ because the clear histogram boundaries have not yet fully formed, before this time, the initial already high density at the centre of the current sheet, $n_0 = 37n_b$, is compressed even more in the centres of magnetic islands, as we have already shown in 2D and 3D in both radiative and non-radiative cases (see Sections 4 and 5). By the time the diagnostic becomes available around $t \sim 1L_y/c$, the density has already compressed to peak values as high as $n/n_b \sim 80$ ($n/n_0 \sim 2$) and the peak density has already begun to decrease. For all 3D cases the degree of density compression in Fig. 15(a) drops as a function of time due to kinking (see Section 5.2 and Appendix B). Meanwhile, the magnetic field, which has also already started compressing, continues to grow, as seen in Fig. 15(b).

We can measure the dependence of the compression on the strength of radiative cooling, controlled by the strength of the upstream reconnecting field B_0/B_Q, by comparing our three simulations. We find that both $\max(n)/n_b$ and $\max(B)/B_0$ have a rather weak dependence on B_0/B_Q in 3D. By $tc/L_y = 3$, the respective enhancements of the compression are ~ 50 per cent and ~ 30 per cent in the radiative case compared to the classical case. Thus, in contrast with the 2D results from Schoeffler et al. (2019), the radiative cooling-driven enhancement is relatively modest. Since the out-of-plane magnetic flux due to the initially relatively strong guide-field $B_G/B_0 = 0.4$ is conserved no matter how strongly the plasma cools radiatively, the compression is limited. However, in 3D, as we show in Section 6.1, the compression is maximized for this value of the guide field. Although the B_0/B_Q-dependence is not so significant (at least for these parameters), we will use these measurements of compression to investigate its dependencies on other parameters in Section 6 and determine in which regimes more compression may be expected.

In summary, in this section, we have shown that, like in 2D, the plasma energization due to 3D relativistic magnetic reconnection leads to a sudden increase in the total radiated power P_{tot} and its simplified fluid-level estimates $P_{\text{tot, est}}$ and $P_{\text{tot, est, 2}}$. This increase is further enhanced by the compression of n and B within the magnetic islands, which we can quantify using theoretical limits in n-B space (where the limit on density is only found in 3D). The compression enhances the emission of energetic photons and thus may be an important factor in powering gamma-ray flares from various astrophysical systems. Simulations performed in 2D give good qualitative agreement with the 3D simulations in overall particle spectra, the total radiation power, and field maps. However, the much stronger density compression, and thus also local emissivity enhancement, found in 2D are disrupted by kinking instabilities that can (and do) develop only in 3D simulations. Although the density compression is reduced in 3D relative to the 2D case, the sudden increase in radiative power persists.

6 PARAMETER SCANS

Significant synchrotron gamma-ray emission (i.e. radiation with photon energies $E_\gamma > m_e c^2$) occurs when the parameter χ_e of a significant number of particles gets as large as $\chi_e \sim 1/\gamma$, and thus the synchrotron photon energy, which is about $\hbar(eB/m_e c)\gamma^2$ is of the order of $m_e c^2$. Reconnection can cause an enhancement of the χ_e parameter by particle energization and also by magnetic field compression.

In Sections 4 and 5, we have found that, although larger values of B_0/B_Q lead to more intense gamma-ray emission, the enhancement of radiation from the reconnection process becomes less pronounced for stronger magnetic fields, due to radiative cooling of the plasma overall, as well as the fact that locations of most significant radiation also suffer the most radiative cooling. However, we have also found that radiative cooling leads to an enhanced compression of the magnetic field and plasma density, helping us to mitigate these effects. We have thus begun to understand the effect of one parameter, i.e. the normalized strength of the reconnecting magnetic field B_0/B_Q, on gamma-ray emission. However, there are several other important parameters to consider which also merit investigation.

To decide which parameters to investigate, we consider some important questions. For example, in what parameter regimes do we expect the strongest compression and the strongest flaring of radiation in the gamma-ray energy range? In which regimes do we expect 2D models to provide good predictions for the full 3D system? When are kinking instabilities in the z direction important, and how

do they affect compression? Some regimes exist in theory, but are difficult to simulate numerically; are there regimes with stronger flaring of radiation in the gamma-ray energy range than those we can simulate? In what regime is significant pair production eventually expected to take place (i.e. typically $\chi_e > 1$)? Do we expect such regimes to occur in astrophysical environments?

Motivated by these questions, in this section we will explore the effects of several important parameters: guide field (B_G/B_0), which resists and inhibits compression but can also mitigate 3D effects by suppressing the kinking instabilities; system size (L_y/ρ_L and L_z/ρ_L), which allows for longer evolution of both relevant 2D and 3D dynamics; and upstream plasma magnetization σ_h, which quantifies the magnetic energy released during reconnection. Each of the subsections that follow presents the findings of an individual parameter scan with respect to one of these parameters. We perform these parameter scans by starting with our previous fiducial case, the 3D radiative ($B_0/B_Q = 4.53 \times 10^{-3}$) simulation setup, and individually varying these parameters while keeping the others constant.

6.1 Parameter scan: guide field B_G

The first step towards finding a regime with significant gamma-ray emission is looking at the dependence on the guide field B_G/B_0. A real 3D plasma acts like a 2D simulation only for a sufficiently strong guide field. Therefore, one should view as tentative any conclusions based on 2D simulations with a weak guide field, such as those presented by Schoeffler et al. (2019), where the compression was unphysically large. For the simulations shown in the previous sections of this paper, we have chosen a guide field of $B_G/B_0 = 0.4$, which is both strong enough for an order-of-magnitude agreement with 2D simulations, but also weak enough to allow significant compression and thus enhancement of emitted radiation power.

To investigate the dependence of the results on the guide field, we have performed a parameter scan of $B_G/B_0 = 0.05, 0.2, 0.4, 0.6$, and 1.0, for the 3D radiative case, keeping $B_0/B_Q = 4.53 \times 10^{-3}$, $L_y/\rho_L = L_x/\rho_L = 314.4$, $L_z = 0.19\,L_y = 58.6\rho_L$, and $\sigma_h = 25.76$ fixed.

We again use the histogram diagnostic from Section 3.2 to find a good measure of the maximal n and B compression for times $t > L_y/c$ after the clear boundaries have developed. We show in Fig. 16(a) that the compression of the magnetic field has a clear dependence on the strength of the guide field. Here we calculate the compression based on the maximal total field compared to the initial upstream total field $|\boldsymbol{B}_0 + \boldsymbol{B}_G|$, instead of just B_0, as we are no longer keeping B_G constant. One should first note that the effect of the guide field on the magnetic compression is non-monotonic. While for strong guide fields e.g. $B_G/B_0 = 1$, the guide-field pressure naturally acts to limit the compression of the plasma and thus the compression of the magnetic field, for a very weak guide field $B_G/B_0 = 0.05$ there is also almost no compression seen. As we will show later in this subsection, the compression, in this case, is disrupted by the development of a kink instability. We thus find that magnetic-field compression peaks at intermediate guide fields, $B_G/B_0 = 0.2 - 0.4$. For these guide fields, the compression fluctuates strongly in time but, on the whole, continues to grow up to $tc/L_y \approx 3$. At this time the compression is strongest for $B_G/B_0 = 0.4$, justifying our choice of this value of B_G for our main fiducial simulations. A similar trend was found by Cerutti et al. (2014b), where non-thermal particle acceleration was also maximized at these moderate guide-field strengths.

As for the compression of the plasma density, we see a similar non-monotonic trend. Fig. 16(b) shows a clear dependence on B_G at the earliest time that the density compression diagnostic is available, e.g.
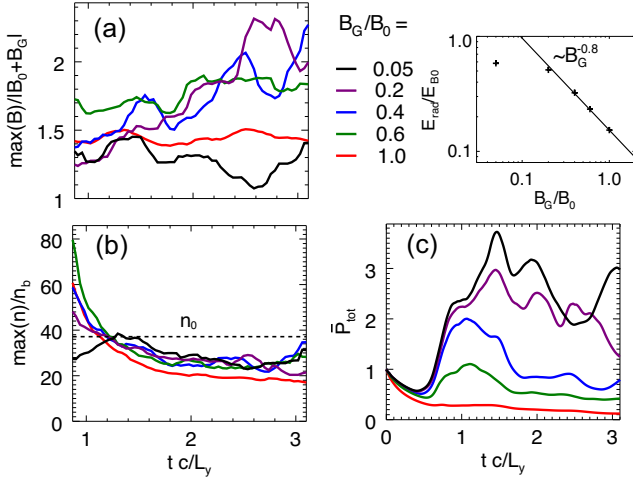
Figure 16. Peak (a) magnetic field, normalized to the initial upstream field strength $(B_0^2 + B_G^2)^{1/2}$, and (b) plasma density, corresponding to the upper right vertex of the best-fitting polygon boundary of the *n-B* histogram (see Section 3.2), and (c) total normalized radiated power $\bar{P}_{\text{tot}}$ (with the time-integrated power as a function of B_G/B_0 plotted above), as functions of time for 3D radiative simulations with a range of initial guide magnetic fields: $B_G/B_0 = 0.05$ (black), 0.2 (magenta), 0.4 (blue), 0.6 (green), and 1.0 (red). The dotted line in panel (b) is the initial density at the centre of the Harris current layer.

at $tc/L_y \approx 1$, where it is largest for a guide field $B_G/B_0 = 0.6$. Soon thereafter, however, the dependence becomes less clear, with the differences between all the curves except the red one ($B_G/B_0 = 1.0$) being comparable to their fluctuation level. The density compression then rises somewhat for some of the simulations just before the end of the runs, and reaches a maximum at $tc/L_y \approx 3$, occurring at $B_G/B_0 = 0.4$, similar to the magnetic compression. One can note that the red line ($B_G/B_0 = 1.0$) is consistently below all others starting from about $tc/L_y \approx 1.2$; i.e. that a strong guide field does suppress compression of the plasma. This suppression eventually leads to a compression smaller than in the case with the strongest compression by almost a factor of 2.

One should note that although the compression is suppressed in weak guide fields, the total radiated power increases as B_G is lowered, see Fig. 16(c). The total energy E_{rad} radiated up to $t_{\text{max}} = 3.16L_y/c$, obtained by integrating the radiated power from Fig. 16(c) up to this time, normalized to the initial energy contained in the reconnecting magnetic field E_{B0}, is plotted as a function of B_G/B_0 in the top right-hand panel of Fig. 16, just above panel (c). As one might expect, the radiated energy does not depend strongly on the guide field when the guide field is weak, $B_G \lesssim 0.2B_0$. For low B_G/B_0 approaching 0, the energy radiated approaches $E_{\text{rad}} \approx 0.6$. However, there is a clear power-law dependence for stronger guide fields, scaling inversely with B_G/B_0 [as $\sim(B_G/B_0)^{-0.8}$]. This is because the reconnection rate becomes smaller for higher B_G/B_0, and thus there is less energy dissipation and hence less radiation. However, we find that the local average values of χ_e or $\gamma \chi_e$ increase with the magnetic compression. Therefore, the largest values occur in the simulation with maximal compression ($B_G/B_0 = 0.4$).

The physical origin of these numerically observed trends, in particular, the suppression of the compression of plasma and magnetic fields in the weak guide-field regime in 3D, can be traced to the effect that the guide field has on the 3D instabilities developing in the current sheet. The initial current sheet is unstable to two types of modes; the tearing mode developing primarily in the $\hat{x}$ direction and

the RDKI mode primarily in the $\hat{z}$ direction. To identify the dominant modes, we use fast Fourier transform (FFT) of the density maps from the PIC simulations of this B_G parameter scan at a relatively early time $tc/L_y \approx 0.4$. We find the peaks of the Fourier power spectrum at $\boldsymbol{k}\rho_L \approx [0.2, 0, 0]$ ($\boldsymbol{k}\delta \approx [0.5, 0, 0]$) for the tearing mode and $\boldsymbol{k}\rho_L \approx [0, 0.34, 0.2]$ ($\boldsymbol{k}\delta = [0, 0.87, 0.5]$) for the kink mode. Here the component of the wavenumber directed in the $\hat{y}$ direction just corresponds to the thickness of the unstable current sheet and is not associated with the direction of the unstable mode.

Figs 17(a)–(e) shows early-time, $t \approx 0.6L_y/c$, 3D renderings of the plasma density contours, which exhibit kinking across a range of guide fields, with decreasing amplitude as the guide field increases. At a slightly earlier time $tc/L_y \approx 0.4$, the calculated FFT of the density in the (k_x, k_z) space at fixed $k_y\rho_L = 0.34$ in Figs 17(f)–(j) shows the presence of both tearing and kinking modes (although the tearing mode peaks at $k_y = 0$, it is still visible at $k_y\rho_L = 0.34$). The tearing mode is slowed down but not fully suppressed by the guide field and is found for all the parameters that we have investigated. It is therefore important to understand the role of the kinking modes which, when significant (for weak guide fields), act to disrupt the compression of the plasma and magnetic fields observed in 2D. We find that the kinking mode, which is only found in 3D where $k_z \neq 0$, disrupts and limits the compression seen in 2D simulations, and thus explains why the density compression max $(n)/n_b$ depends strongly on B_G/B_0 at $tc/L_y \approx 1$, shown in Fig. 16(b). As one can see in Figs 17(f)–(j), the kink's amplitude is highest for the weakest $B_G/B_0 = 0.05, 0.2$. As B_G/B_0 is increased, this mode is suppressed, growing slower and saturating earlier. For $B_G/B_0 = 1.0$, the kinking mode is completely suppressed for our fiducial value of L_z [no kinking mode is visible in the Fourier spectrum in Fig. 17(j)]. While the dominant kinking mode at early stages is the RDKI mode with a fixed wavelength in the $\hat{z}$ direction, $\lambda = 2\pi k_z^{-1} \sim 30\rho_L$, at later times the MHD kink instability of the flux ropes starts to dominate. The corresponding dominant MHD kink mode's wavelength grows with the guide field and, for our strongest guide-field case $B_G/B_0 = 1.0$, it can only fit in boxes with L_z larger than simulated in the present parameter scan. We will explore the L_z-dependence of both of these 3D kinking modes in the next subsection.

To sum up, the maximum compression in our 3D reconnection simulations occurs at intermediate values of the guide field, e.g. $B_G/B_0 \approx 0.4$, when the compression-disrupting kinking instabilities are somewhat suppressed by the guide field, but, at the same time, the guide-field's pressure $B_G^2/8\pi$ is not strong enough to prevent the compression outright.

6.2 Parameter scan: L_z

As shown in the previous subsection, stronger guide fields suppress variations in the $\hat{z}$ direction, in particular those coming from the kinking modes, making 3D results more like 2D. In general, 3D simulations become more accurate when the box size $2L_z$ in the guide-field direction (quantified by L_z/ρ_L or L_z/L_y) is increased, allowing for modes with longer wavelengths and more variations to fit in the $\hat{z}$ direction. An important question is: for a given guide field, how large does L_z/ρ_L (or L_z/L_y) need to be to capture the relevant 3D physics? From the previous subsection, we learned that, for moderate guide fields, at least the initially dominant $k_z\rho_L \approx 0.2$ RDKI mode of the initial Harris current sheet, with wavelength $\lambda = 2\pi/k_z \simeq 30\rho_L$, has to fit in the box of length $2L_z$. Our main fiducial sequence of 3D runs in Section 5 adopted the z-length $L_z = 58.6\rho_L = 0.19L_y$. This is sufficiently long to resolve four initial wavelengths ($k_z 2L_z/2\pi \approx 4$), and thus these initial RDKI kinking modes are well
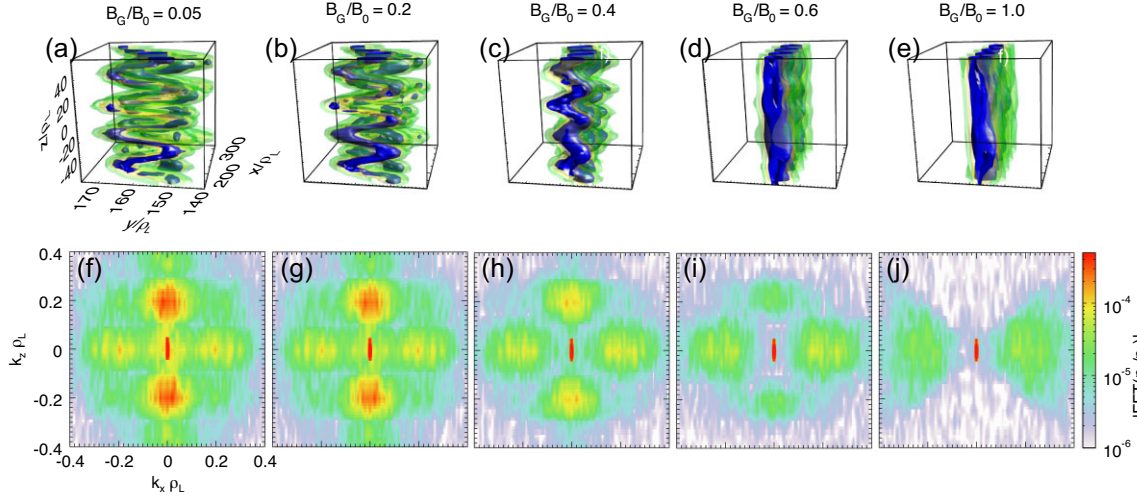
Figure 17. 3D renderings of density contours (top row: panels a–e) at $tc/L_y = 0.566$ and the spatial Fourier decomposition of the density (bottom row: panels f–j) at $tc/L_y = 0.404$, for 3D radiative-case simulations with different guide-field strengths: from left to right, $B_G/B_0 = 0.05, 0.2, 0.4, 0.6$, and 1.0. Bottom-row panels (f–j) are 2D cuts of the 3D FFT at $k_y\rho_L = 0.34$.

captured. In the present subsection, we justify our choice for L_z, by comparing simulations with a range of lengths.

We performed a parameter scan of $L_z/\rho_L = 7.325, 14.65, 29.3, 58.6, 117.2$, and 175.84, keeping $B_0/B_Q = 4.53 \times 10^{-3}$ (i.e. radiative case), $B_G/B_0 = 0.4$, and $\sigma_h = 25.76$ fixed. For computational reasons, these simulations were done using a smaller system size $L_x/\rho_L = L_y/\rho_L = 157.2$ (i.e. half of our fiducial system size); this allowed us to explore a broad range of aspect ratios from $L_z/L_y = 0.047$ to 1.125. Unfortunately, at this smaller system size, there is not much space and time for significant compression.

We find that only the biggest-L_z/ρ_L runs have *n-B* histograms that resemble those for the 3D runs presented in Section 5 and allow for the use of the compression diagnostic from Section 3.2. As we see in Figs 18(a)–(c), the histograms of the runs with the smallest values of $L_z/\rho_L \in [7.3, 14.7, 29.3]$ resemble those from the 2D simulations [see Fig. 6(b)], where B/B_0 follows the frozen-in scaling of equation (19) for $n/n_b < 1$ and continues to increase with n for $n/n_b > 1$, with a weaker slope. On the other hand, in larger-L_z simulations ($L_z/\rho_L > 30$; $L_z/L_y > 0.19$), shown in Figs 18(d)–(f), the histograms more strongly resemble those from the fiducial 3D simulations of Section 5 [see Fig. 12(b)]. In particular, while the bulk of the background plasma still follows the frozen-in scaling of equation (19), there are clear and distinct power-law boundaries above and to the right of the distributions. This allows us to employ our standard measures of maximal density and magnetic-field compression (see Section 3.2) in terms of the intersection point of these histogram boundaries [red plus signs in Figs 18(d)–(f)].

As seen in Figs 19(a) and (b), the compression in both *n* and *B* (from the histogram diagnostic in Section 3.2) is not as strong as that found in the simulations with larger L_y. However, we can conclude that while the dependence on L_z is not strong, the compression may be still slightly greater for larger L_z. The normalized emitted power $\bar{P}_{tot}$, shown in Fig. 19(c), is greater for the simulations with the smallest values of L_z, which are essentially 2D runs, while for $L_z/\rho_L > 30$ the emitted power appears to become independent of L_z.

As in the previous subsection 6.1, we show early-time 3D isocontours of the density at $tc/L_y = 0.566$ in Figs 20(a)–(f) and the FFT of the density in the *xz* plane (at $k_y\rho_L = 0.34$) at $tc/L_y = 0.404$ in Figs 20(g)–(l), now for several values of L_z/ρ_L. The initial
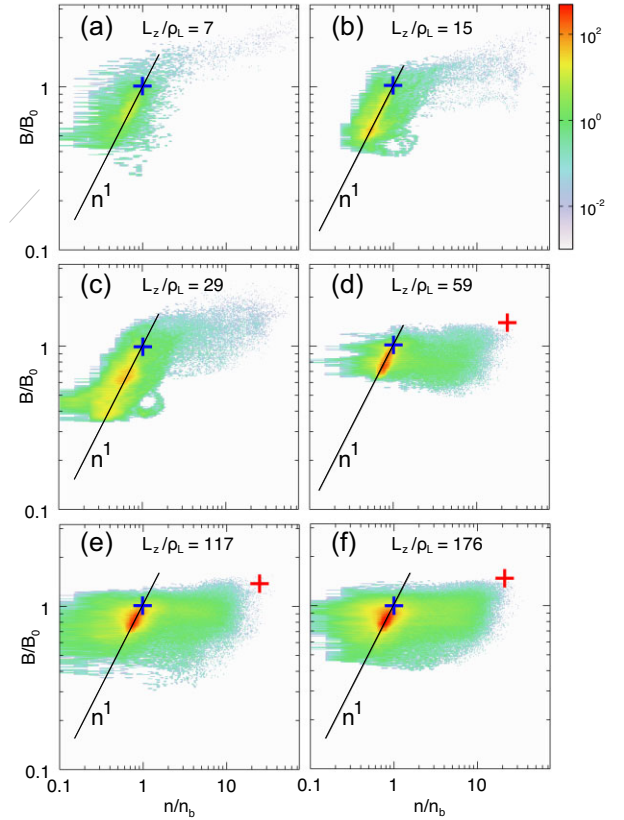
Figure 18. Histograms in *n-B* space in terms of the local density n/n_b and magnetic field B/B_0 at $t = 3L_y/c$ for the 3D radiative-case simulations with different L_z: $L_z/\rho_L = (a)$ 7.3, (b) 14.7, (c) 29.3, (d) 58.6, (e) 117, and (f) 176. The blue plus signs represent the initial conditions of the upstream background, the red plus signs represent the upper right vertex of the best-fitting polygon boundary (see Section 3.2), which is plotted versus time in Fig. 19. The $B \sim n$ scaling [equation (19)] is shown with thin solid lines.
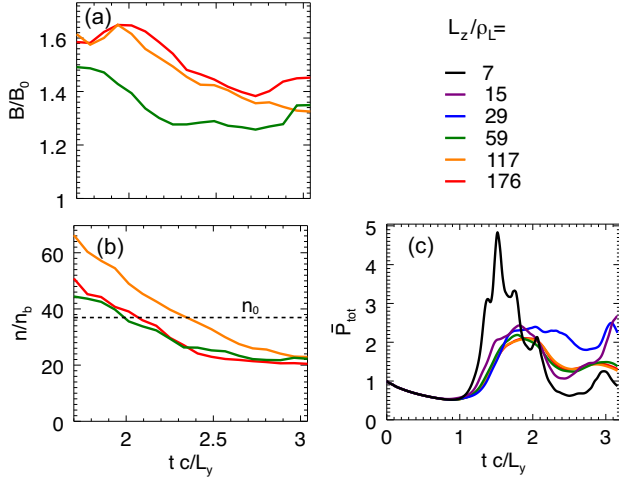
Figure 19. Peak (a) magnetic field and (b) plasma density at the upper right vertex of the best-fitting polygon boundary (see Section 3.2), indicated with the red plus signs in Fig. 18, along with (c) total normalized emitted power $\bar{P}_{\text{tot}}$, as functions of time for the 3D radiative-case simulations with $L_x = L_y = 157.2\,\rho_L$ and with a range of system sizes in the $\hat{z}$ direction: $L_z/\rho_L = 7.3$ (black), 14.7 (magenta), 29.3 (blue), 58.6 (green), 117 (orange), and 176 (red). The dotted line in panel (b) is the initial density at the centre of the Harris current layer.

kinking mode appears at the same value of $k_z\rho_L \simeq 0.2$ as in the previous subsection, independent of L_z, for all the runs except for the quasi-2D case $L_z/\rho_L = 7.3$. The reason why there are no signs of the kinking mode in the $L_z/\rho_L = 7.3$ case is simply that the wavelength of this instability mode, $\lambda_z/\rho_L \sim 30$, is too long to fit in the box of a full z-extent of $2L_z \simeq 15\rho_L$. On the other hand, our fiducial choice of the box half-length $L_z = 58.6\rho_L$ captures almost four full wavelengths. Besides this main RDKI kinking mode, we do not see any other significant variations along the $\hat{z}$ direction, e.g. any clear evidence of the MHD kink modes, at this relatively early time, even for the largest value of $L_z/\rho_L = 176$ ($L_z/L_y = 1.12$, four times longer than our fiducial L_z). Therefore, $L_z/\rho_L = 58.6$ ($L_z/L_y = 0.37$) appears to be sufficient to capture the 3D effects, at least at early times. It is still not clear if 3D effects might become more important at higher values of L_y/ρ_L or L_z/L_y, which we did not simulate in this study. As

we discussed in Section 5.2, the peak density of the current filaments appears to be limited at late times to a certain region in n-B space, governed by the marginal stability condition for the flux-rope kink mode in the filaments, and this may explain the lack of clear kinking modes.

We thus conclude that, although rough, order-of-magnitude predictions of compression and radiation are possible based on 2D simulations, an accurate prediction in 3D requires the domain's length in the third dimension to be large enough to capture at least the initial RDKI instability.

6.3 Parameter scan: L_y

Other parameters may lead to stronger compression, greater χ_e, and thus more powerful emission of gamma-rays, but are also more computationally difficult to study. In particular, in this subsection, we consider the dependence on the system size L_y/ρ_L. Increasing the system size leads to a longer time of evolution of plasmoids, and thus potentially to stronger compression of the magnetic field in plasmoid cores, and more pronounced non-thermal particle acceleration.

In order to see the effects of system size, we have performed, in addition to our fiducial $L_y/\rho_L = 314.4$ run, two more simulations, with both larger ($L_y/\rho_L = 471.6$) and smaller ($L_y/\rho_L = 157.2$) sizes, keeping $L_z/\rho_L = 58.6$, $B_0/B_Q = 4.53 \times 10^{-3}$, $B_G/B_0 = 0.4$, and $\sigma_h = 25.76$ fixed. The simulation duration was $t_{\max}c/L_y = 3.16$ in all the runs.

We find that the degree of compression (from the histogram diagnostic in Section 3.2) scales with the time normalized to the (microscopic) cyclotron time-scale $c/\rho_L = \gamma_T\,\Omega_c^{-1}$, rather than to the (macroscopic) system's light-crossing time c/L_y. Therefore, in Fig. 21, we show the comparisons of the time histories of the magnetic field (panel a) and density (panel b) compression, as well as of the total normalized power (panel c), using this microscopic time normalization, which indicates little dependence on the system size. However, while the level of compression in n seems to reach an approximate steady state at late times that is weakly dependent on system size, the compression of B appears to continue to grow roughly linearly with time. Therefore, for simulations with a given duration in light-crossing times, magnetic compression can eventually reach larger values for larger system sizes. Note that for the smallest system size ($L_y/\rho_L = 157.2$) there is not enough time for
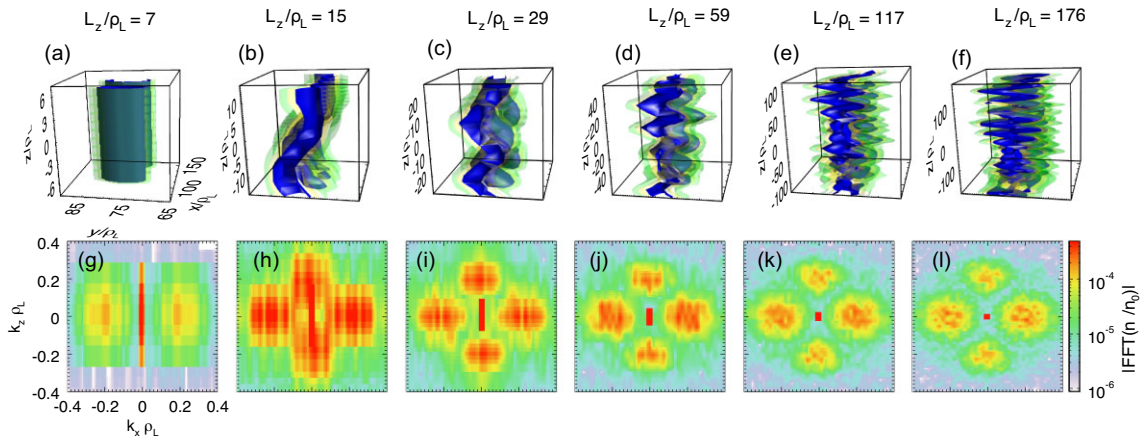
Figure 20. 3D renderings of density contours (top row: panels a–f) at $tc/L_y = 0.566$ and the spatial Fourier decomposition of the density (bottom row: panels g–l) at $tc/L_y = 0.404$, for 3D radiative-case simulations with different $L - z$: from left to right, $L_z/\rho_L = 7.3$, 14.7, 29.3, 58.6, 117, and 176. Bottom-row panels (g–l) are 2D cuts of the 3D FFT at $k_y\rho_L = 0.34$.
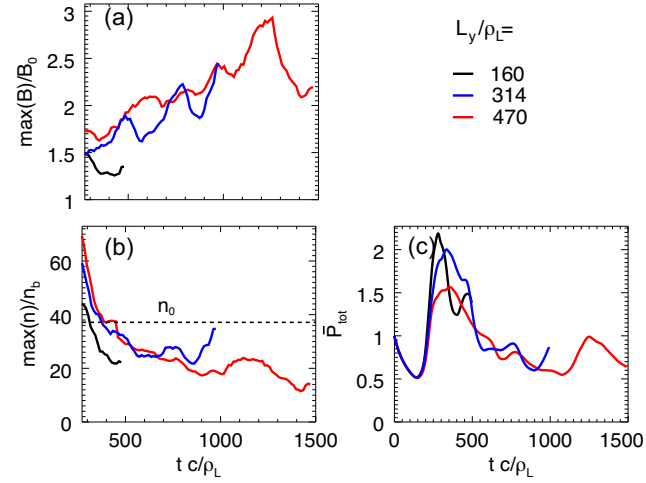
Figure 21. Peak (a) magnetic field and (b) plasma density at the upper right vertex of the best-fitting polygon boundary (see Section 3.2), and (c) total normalized emitted power $\bar{P}_{\text{tot}}$, as functions of time for 3D radiative-case simulations with a range of system sizes: $L_y/\rho_L = 157.2$ (black), 314.4 (blue), and 471.6 (red). The dotted line in panel (b) is the initial density at the centre of the Harris current layer.

significant compression, and hence the magnetic compression does not exhibit a clear linear trend like in the other two cases.

Like the density compression, the total normalized emitted power $\bar{P}_{\text{tot}}$ decreases as a function of time at intermediate times and approaches a steady state at late times [see Fig. 21(c)]. In general, more power is emitted at relatively early times, $tc/\rho_L \sim 300 - 500$. However, for larger system sizes, there is more time for the compressed magnetic field and increased temperature (not shown) to lead to more energy radiated at higher photon energies. Therefore, larger systems have greater potential for producing brighter gamma-ray emission and hence possibly more copious pair production.

6.4 Parameter scan: σ_h

Although large-σ_h simulations are computationally challenging, because it is numerically difficult to handle initial Harris equilibria with very large density contrasts n_0/n_b (a force-free initial equilibrium may be more amenable to simulation studies in this regime), these parameter regimes may be more relevant to astrophysical environments associated with gamma-ray flares. We, therefore, look at the dependence of some of the key reconnection characteristics on the magnetization σ_h. As a reminder, this parameter quantifies the relative free energy in the upstream magnetic fields that can be converted by reconnection into plasma heating and the non-thermal acceleration of particles. For high σ_h, the magnetic pressure dominates over the plasma pressure, potentially enabling stronger density compression. Therefore, as σ_h is increased, we expect to find both greater heating and acceleration, and stronger compression of plasma density, leading to higher χ_e and thus brighter gamma-ray emission.

We have performed a parameter scan of $\sigma_h = 6.44$, 12.88, and 25.76, keeping $T_b = 4m_e c^2$, $B_0/B_Q = 4.53 \times 10^{-3}$, $B_G/B_0 = 0.4$, $L_z/\rho_L = 58.6$, and $L_x/\rho_L = L_y/\rho_L = 314.4$ constant. The magnetization $\sigma_h \sim 1/n_b$ is varied by changing n_b while keeping the other two basic background plasma parameters, T_b and B_0, constant. We also keep fixed most of the initial parameters of the current sheet, namely, its initial thickness $\delta = 2.55\rho_L$ and temperature $T_0 = 6.92m_e c^2$, as well as the drift velocity $v_d/c = 0.56$ of current-carrying particles [see equation (A8) in Appendix A]. This, in turn, implies
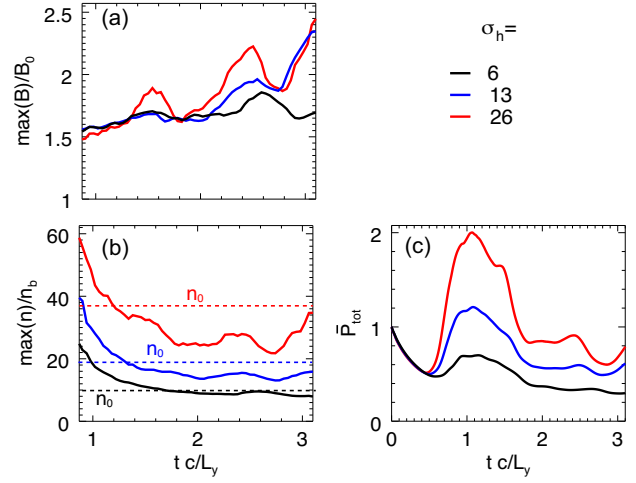

Figure 22. Peak (a) magnetic field and (b) plasma density at the upper right vertex of the best-fitting polygon boundary (see Section 3.2), and (c) total normalized emitted power $\bar{P}_{\text{tot}}$, as functions of time for 3D radiative-case simulations with a range of upstream magnetizations: $\sigma_h = 6.44$ (black), 12.88 (blue), and 25.76 (red). The dotted lines in panel (b) are the initial densities at the centre of the Harris current layer.

that the difference in density $n_0 - n_b$ is kept constant [equation (A7) in Appendix A] as σ_h (and hence n_b) is varied, and so n_0 is changed slightly. The respective density contrasts for increasing σ_h are $n_0/n_b = 10$, 19, and 37.

Again, we examine the compression from the histogram diagnostic in Section 3.2, after $t = L_y/c$, once the distribution has sufficiently mixed. As shown in Fig. 22(a), the magnetic field compression for $\sigma_h \simeq 6.4$ stays nearly constant at a modest value of about (1.6–1.8) throughout the simulation. However, for higher magnetization, $\sigma_h \simeq 13$ and 26, the magnetic compression exhibits an overall growth, up to ~ 2.5 at the end of the simulation, on top of strong fluctuations. Generally, higher σ_h results in stronger magnetic compression. The peak density compared to the initial background density n_b, displayed in Fig. 22(b), is also higher for higher magnetization. However, this dependence does not actually reflect the degree of compression, simply because higher magnetization just corresponds to lower normalization n_b relative to the peak density n_0 in the initial Harris layer. Therefore, comparing the peak density of the compressed regions to n_0 would be a better measure. Although a density compression has clearly occurred by the time the histogram diagnostic is first available [max $(n)/n_0 \sim 2$ at $t \approx L_y/c$], the peak density decreases with time and quickly drops below n_0, especially for higher σ_h. After that, during the second half of each simulation ($t \gtrsim 1.5 L_y/c$), the peak density fluctuates below n_0, around a saturated level that decreases, when normalized to n_0, as σ_h is increased, see Fig. 22(b). Since the late-time peak density remains below n_0 for all cases, any sustained compression can only be due to the background plasma, rather than the plasma from the initial current sheet.

Taking into account the magnetic field compression, we expect an overall increase in the values of χ_e for typical particles in magnetic islands, which would be consistent with the clear enhancement of the normalized radiated power for increased values of σ_h seen in Fig. 22(c). Note that although there is a greater enhancement of normalized radiated power for higher σ_h, the total energy radiated by the end of the simulations remains about 1/3 of the initial energy in the reconnecting field for all σ_h. The initial radiated power decreases with σ_h, because there are fewer radiating particles in the background.
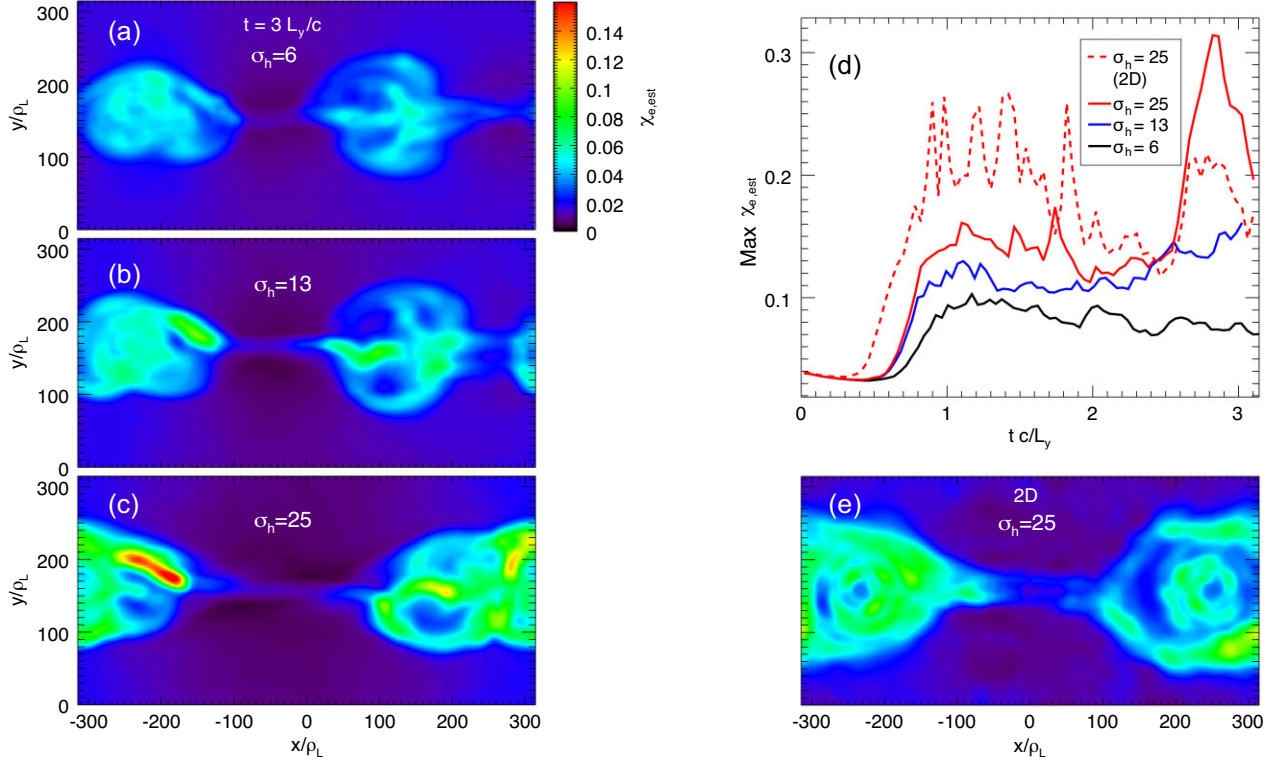
Figure 23. 2D maps of estimated local averaged $\chi_{e,\text{est}} \equiv (2T/m_ec^2)(B/B_Q)$ at $t = 3L_y/c$ from a representative $z = 0$ cut for 3D radiative-case simulations with (a) $\sigma_h = 6.44$, (b) 12.88, and (c) 25.76. Panel (d) shows the time evolution of the maximum $\chi_{e,\text{est}}$ for each of the simulations. Panel (e) shows the $\chi_{e,\text{est}}$-map from the 2D radiative case with $\sigma_h = 25.76$.

A very good estimation for the average χ_e of particles at a given location is given by $\chi_{e,\text{est}} \equiv (2T/m_ec^2)(B/B_Q)$, shown in Fig. 23. A comparison of the 2D maps of this quantity, corresponding to the slices of the simulation domain at $z = 0$ at $t = 3L_y/c$, illustrates the expected increase in χ_e with increased σ_h, as seen in Figs 23(a)–(c). In addition to these maps, the dependence of $\chi_{e,\text{est}}$ on σ_h is clearly visible in the time histories of the maximum (over the domain) values of $\chi_{e,\text{est}}$, plotted in Fig. 23(d). For the $\sigma_h = 25.76$ case (the radiative case in Section 5), the maximum local average $\chi_{e,\text{est}}$ grows rapidly before plateauing at about 0.15 (i.e. somewhat below the 0.2–0.25 range of variation found in the corresponding 2D simulation). It then fluctuates around this level throughout most of the active reconnection phase, before spiking suddenly near the end of the simulation to a value as high as 0.3, almost a factor of 10 higher than the initial background value of 0.038 [see Fig. 23(d)]. Although the total radiated power in 3D is not a high as in 2D [the radiative case in Section 4], the high values that $\chi_{e,\text{est}}$ reaches in 3D at late times [see Fig. 23(c)] exceed those seen in the 2D case with the same $\sigma_h \approx 26$ [see Fig. 23(e) and the red dashed line in Fig. 23(d)].

We have thus shown that the initial background magnetization σ_h has a significant effect on the magnetic field and density compression, the total emitted power, and the average χ_e parameter in the cores of plasmoids, all pointing to regimes where gamma-ray emission can be more efficient.

7 CONCLUSIONS

We have presented the results of a comparative 2D and 3D numerical study of collision-less relativistic reconnection of strong magnetic fields in an electron–positron pair plasma, self-consistently taking into account synchrotron radiation reaction. The main focus of our study was on investigating reconnection-powered sudden bursts of enhancement of the estimated local emissivity ϵ_{est} and the total radiated power P_{tot}, especially in the gamma-ray regime. Our radiative-PIC simulations were conducted with the OSIRIS radiative-PIC code and were initialized with a self-consistent equilibrium relativistic, dense Harris sheet immersed in a lower density ambient background pair plasma. We have investigated the effects of the relative strength of synchrotron cooling, controlled by the reconnecting magnetic field B_0/B_Q, in both 2D (Section 4) and 3D (Section 5). In addition, in 3D, we have performed an extensive study of the effects of several other key physical parameters (Section 6), namely, the relative strength of the non-reconnecting, guide magnetic field along the $\hat{z}$ direction B_G/B_0 (Section 6.1), the length of the current sheet in the $\hat{z}$ direction L_z/ρ_L (Section 6.2), which characterizes 3D effects, the system size in the perpendicular direction L_y/ρ_L (Section 6.3), and the upstream plasma magnetization σ_h (Section 6.4).

We have developed two novel diagnostic estimates of the total radiated power, which also help elucidate what causes the bursts in photon emission found in both 2D and 3D simulations. These diagnostics are based on fluid-level quantities obtained as reductions of the PIC-simulation kinetic data. The first one is a simple estimate of radiated power $P_{\text{tot, est}}$ [equation (17)], which integrates the estimated local emissivity ϵ_{est}, ignoring both bulk-flows and kinetic effects/non-Maxwellian distributions; it eventually overestimates the emission of radiation (for more radiative cases), but takes into account the important correlation between the magnetic energy density and plasma energy density. The second estimate, $P_{\text{tot, est2}}$ [see equation (18)], is even simpler, as it ignores this correlation, and thus underestimates the emission. We have found that reconnection

naturally leads to the development of inhomogeneities in the system, e.g. via plasma and magnetic-field compression inside plasmoids (magnetic islands; or flux ropes in 3D). The resulting increased values of the plasma density, magnetic field, and temperature are, in general, spatially correlated and found concentrated in plasmoid cores. This enhancement and correlation, which is taken into account by $P_{\text{tot, est}}$, increases the local emissivity and the total radiated power in comparison with the more naive estimate $P_{\text{tot, est2}}$, especially in 2D. Although, as we had pointed out in our previous paper (Schoeffler et al. 2019), radiative cooling can drive an even stronger compression and hence a further concentration of the radiative regions in the central cores of magnetic islands, making them more effective radiators, in this study we have found that enhanced radiative cooling of the plasma caused by stronger magnetic fields actually reduces the appropriately normalized radiated power.

We have found that, for the most part, 2D simulations yield reasonable qualitative estimates (i.e. within factors ~2) for several key characteristics, such as the radiated power, particle spectra, magnetic field compression, etc., for the full 3D system with a moderate guide field $B_G/B_0 = 0.4$. However, for some other quantities, we have observed rather large differences between 2D and 3D results. For example, the localized compression of plasma density and the enhancement of local emissivity in 2D can reach peak values around a factor of 10 greater than in 3D. Such unphysically strong plasma compression does not occur in 3D because compression becomes disrupted by kinking instabilities, in particular, the RDKI at early times, capturing which requires accessing modes with $k_z\delta \sim 0.5$.

To study the development and limits of compression, and to help highlight the correlations between density n, magnetic field B (and sometimes temperature T) that drive the enhancements of reconnection-powered radiation, we have designed and made use of a novel compression diagnostic based on 2D histograms in n-B and n-T spaces of our simulations (Section 3.2). We have observed that the distributions of points on these histograms, especially in 3D simulations, tend to develop very clear, well-defined borders, described by power laws, corresponding to sharp limits on the compression.

We have presented tentative theoretical explanations for two such compression limits seen on the histograms in our simulations: for the maximum $B/B_0 \sim (n/n_b)^{1/6}$ [equation (D7)] (moderate-density part of the top boundary) for 2D and 3D radiative cases, which we attribute to radiative-resistive dissipation of magnetic fields in secondary plasmoid cores; and (in 3D only) for the maximum density, given by $n/n_b \sim (B/B_0)^1$ [equation (B1)] (right boundary), which appears to be determined by the kink instability condition.

We have further explored the compression and the resulting power radiated using parameter-space scans employing 3D radiative simulations that are subject to both of these compression limits. We have found that the relative enhancement of the radiated power decreases with increased B_G/B_0 or B_0/B_Q but increases significantly with increased magnetization σ_h. The density compression (compared to n_0) does not change significantly for all parameters studied, while the compression of the magnetic fields, on the other hand, increases with B_0/B_Q, L_y/ρ_L, and σ_h.

In light of the results of our study, we expect that magnetic reconnection in strongly radiative, strong-field astrophysical environments is capable of producing bright flares of gamma-rays and X-rays. This study should help us in understanding to what degree these bursts of radiation can explain observations of gamma-ray and X-ray flares, e.g. from the magnetospheres of neutron stars, including magnetars.

In addition, this study paves the way for future numerical 3D investigations of even more extreme astrophysically relevant regimes,

characterized by stronger magnetic fields B_0/B_Q and higher upstream magnetizations σ_h. This will enable us to reach the $\chi_e \sim 1$ regime, where QED effects, including pair creation, can become dominant. Furthermore, extending this study to larger normalized system sizes L_y/ρ_L, in combination with the strong magnetic field, will allow us to reach higher, more realistic values of magnetic compactness ℓ_B, a key parameter governing the importance of radiative and QED effects.

DATA AVAILABILITY

The data underlying this article will be shared on reasonable request to the authors.

REFERENCES

Abbott B. P. et al., 2017, ApJ, 848, L12
Abdo A. A. et al., 2011, Science, 331, 739
Abramowski A. et al., 2012, ApJ, 746, 151
Aharonian F. et al., 2007, ApJ, 664, L71
Albert J. et al., 2007a, ApJ, 665, L51. Available at: https://iopscience.iop.org/article/10.1086/521145
Albert J. et al., 2007b, ApJ, 669, 862
Aleksić J. et al., 2011, ApJ, 730, L8
Beloborodov A. M., 2017, ApJ, 850, 141
Berger E., 2014, ARA&A, 52, 43
Bhattacharjee A., Huang Y.-M., Yang H., Rogers B., 2009, Phys. Plasmas, 16, 112102
Buehler R., Blandford R., 2014, Rep. Prog. Phys., 77, 066901
Cerutti B., Uzdensky D. A., Begelman M. C., 2012, ApJ, 746, 148
Cerutti B., Werner G. R., Uzdensky D. A., Begelman M. C., 2013, ApJ, 770, 147
Cerutti B., Werner G. R., Uzdensky D. A., Begelman M. C., 2014a, Phys. Plasmas, 21, 056501
Cerutti B., Werner G. R., Uzdensky D. A., Begelman M. C., 2014b, ApJ, 782, 104
Cerutti B., Philippov A. A., Spitkovsky A., 2016, MNRAS, 457, 2401
Chen A. Y., Uzdensky D., Dexter J., 2023, ApJ, 944, 173
D'Avanzo P. et al., 2018, A&A, 613, L1
Daughton W., 1999, Phys. Plasmas, 6, 1329
Di Matteo T., 1998, MNRAS, 299, L15
Duncan R. C., Thompson C., 1992, ApJ, 392, L9
Eckart C., 1940, Phys. Rev., 58, 919
Fonseca R. A. et al., 2002, OSIRIS: A Three-Dimensional, Fully Relativistic Particle in Cell Code for Modeling Plasma based Accelerators. Vol. 2331, Springer, Berlin / Heidelberg
Giannios D., 2008, A&A, 480, 305
Giannios D., 2010, MNRAS, 403, L51
Giannios D., 2013, MNRAS, 431, 355
Giannios D., Uzdensky D. A., 2019, MNRAS, 484, 1378
Giannios D., Uzdensky D. A., Begelman M. C., 2009, MNRAS, 395, L29
Goldstein A. et al., 2017, ApJ, 848, L14

Goodbred M., Liu Y.-H., 2022, Phys. Rev. Lett., 129, 265101

Grismayer T., Vranic M., Martins J. L., Fonseca R. A., Silva L. O., 2016, Phys. Plasmas, 23, 056706

Grismayer T., Vranic M., Martins J. L., Fonseca R. A., Silva L. O., 2017, Phys. Rev. E, 95, 023210

Hakobyan H., Philippov A., Spitkovsky A., 2019, ApJ, 877, 53

Hakobyan H., Philippov A., Spitkovsky A., 2023a, ApJ, 943, 105

Hakobyan H., Ripperda B., Philippov A. A., 2023b, ApJ, 943, L29

Harris E. G., 1962, Il Nuovo Cimento (1955-1965), 23, 115

Jaroschek C. H., Hoshino M., 2009, Phys. Rev. Lett., 103, 075002

Jaroschek C. H., Lesch H., Treumann R. A., 2004, ApJ, 605, L9

Kaspi V. M., Beloborodov A. M., 2017, ARA&A, 55, 261

Kirk J. G., Skjæraasen O., 2003, ApJ, 591, 366

Krall N., Trivelpiece A., Kempton J., 1973, Principles of Plasma Physics. International series in pure and applied physics. McGraw-Hill, New York. Available at: https://books.google.pt/books?id = b0BRAAAAMAAJ

Landau L. D., Lifshitz E. M., 1975, The Classical Theory of Fields. Pergamon Press, Oxford

Loureiro N. F., Schekochihin A. A., Cowley S. C., 2007, Phys. Plasmas, 14, 100703

Lyubarskii Y. E., 1996, A&A, 311, 172

Lyutikov M., 2003, MNRAS, 346, 540

Lyutikov M., Komissarov S., Sironi L., Porth O., 2018, J. Plasma Phys., 84, 635840201

Madejski G. G., Sikora M., 2016, ARA&A, 54, 725

Markwardt C. B., 2009, in Bohlender D. A., Durand D., Dowler P.eds, ASP Conf. Ser. Vol. 411, Astronomical Data Analysis Software and Systems XVIII. Astron. Soc. Pac., San Francisco, p. 251

Mazets E. P., Cline T. L., Aptekar' R. L., Butterworth P. S., Frederiks D. D., Golenetskii S. V., Il'Inskii V. N., Pal'Shin V. D., 1999, Astron. Lett., 25, 628

McKinney J. C., Uzdensky D. A., 2012, MNRAS, 419, 573

Mehlhaff J. M., Werner G. R., Uzdensky D. A., Begelman M. C., 2020, MNRAS, 498, 799

Mehlhaff J. M., Werner G. R., Uzdensky D. A., Begelman M. C., 2021, MNRAS, 508, 4532

Melzani M., Winisdoerffer C., Walder R., Folini D., Favre J. M., Krastanov S., Messmer P., 2013, A&A, 558, A133

Mészáros P., 2006, Rep. Progr. Phys., 69, 2259

Nalewajko K., Giannios D., Begelman M. C., Uzdensky D. A., Sikora M., 2011, MNRAS, 413, 333

Nalewajko K., Begelman M. C., Cerutti B., Uzdensky D. A., Sikora M., 2012, MNRAS, 425, 2519

Nalewajko K., Yuan Y., Chruślińska M., 2018, J. Plasma Phys., 84, 755840301

Palmer D. M. et al., 2005, Nature, 434, 1107

Petropoulou M., Giannios D., Sironi L., 2016, MNRAS, 462, 3325

Philippov A., Kramer M., 2022, ARA&A, 60, 495

Philippov A. A., Spitkovsky A., 2018, ApJ, 855, 94

Piran T., 2005, Rev. Mod. Phys., 76, 1143

Pritchett P. L., Coroniti F. V., 2004, J. Geophys. Res.: Space Phys., 109, A01220

Remillard R. A., McClintock J. E., 2006, ARA&A, 44, 49

Romanova M. M., Lovelace R. V. E., 1992, A&A, 262, 26

Schoeffler K. M., Grismayer T., Uzdensky D., Fonseca R. A., Silva L. O., 2019, ApJ, 870, 49

Sironi L., Beloborodov A. M., 2020, ApJ, 899, 52

Sironi L., Petropoulou M., Giannios D., 2015, MNRAS, 450, 183

Sironi L., Giannios D., Petropoulou M., 2016, MNRAS, 462, 48

Spitzer L., Härm R., 1953, Phys. Rev., 89, 977

Sridhar N., Sironi L., Beloborodov A. M., 2021, MNRAS, 507, 5625

Tanaka Y. T. et al., 2011, ApJ, 733, 19

Tavani M. et al., 2011, Science, 331, 736

Uzdensky D. A., 2011, Space Sci. Rev., 160, 45

Uzdensky D. A., 2016, in Gonzalez W., Parker E., eds, Magnetic Reconnection: Concepts and Applications, Vol. 427. Springer, Cham, p. 473

Uzdensky D. A., Spitkovsky A., 2014, ApJ, 780, 3

Uzdensky D. A., Loureiro N. F., Schekochihin A. A., 2010, Phys. Rev. Lett., 105, 235002

Uzdensky D. A., Cerutti B., Begelman M. C., 2011, ApJ, 737, L40

Werner G. R., Uzdensky D. A., 2017, ApJ, 843, L27

Werner G. R., Uzdensky D. A., 2021, J. Plasma Phys., 87, 905870613

Werner G. R., Uzdensky D. A., Cerutti B., Nalewajko K., Begelman M. C., 2016, ApJ, 816, L8

Werner G. R., Uzdensky D. A., Begelman M. C., Cerutti B., Nalewajko K., 2018a, MNRAS, 473, 4840

Werner G. R., Philippov A. A., Uzdensky D. A., 2018b, MNRAS, 482, L60

Zdziarski A. A., Lubiński P., Sikora M., 2012, MNRAS, 423, 663

APPENDIX A: SIMULATION SETUP

In our 2D (3D) simulations, we model a $2L_x \times 2L_y (\times 2L_z)$ domain with two oppositely directed thin current sheets located at $y = \pm L_y/2$. The current is directed out of the (x, y) simulation plane in the respective $\pm \hat{z}$ directions, which leads to an asymptotic magnetic field $\boldsymbol{B} = B_0\hat{\boldsymbol{x}}$, between $-L_y/2 > y > L_y/2$, and $\boldsymbol{B} = -B_0\hat{\boldsymbol{x}}$ on the outside of the two current sheets. An initially uniform background Maxwell-Jüttner population of relativistic electrons and positrons, each with density $n = n_b$ at temperature $T = T_b$, is included to represent the ambient (upstream) plasma. This population is initially stationary and does not contribute to the current. Furthermore, we include a uniform guide magnetic field B_G along the $\hat{z}$ direction.

The current and self-consistent magnetic field profiles are in pressure balance in a kinetic equilibrium, known as the relativistic Harris sheet (Harris 1962; Kirk & Skjæraasen 2003). The current is carried by counter-drifting Maxwell-Jüttner distributions of positrons and electrons with a uniform temperature T_0, boosted into opposite $\pm \hat{z}$-directions with a uniform velocity v_d. The lab-frame density profile (of both electrons and positrons) in the Harris current sheet at $y = \pm L_y/2$ is:

$$n = (n_0 - n_b) \operatorname{sech}^2 \left(\frac{y \mp L_y/2}{\delta} \right), \tag{A1}$$

where n_0 is the total electron (or positron) density at the centre of each current sheet. The self-consistent initial reconnecting magnetic field is:

$$B_x = B_0 \left[1 - \tanh\left(\frac{y - L_y/2}{\delta} \right) + \tanh\left(\frac{y + L_y/2}{\delta} \right) \right. $$
$$\left. + \tanh\left(\frac{y - 3L_y/2}{\delta} \right) - \tanh\left(\frac{y + 3L_y/2}{\delta} \right) \right]. \tag{A2}$$

We conduct our simulations with periodic boundary conditions, so we also include the self-consistent magnetic field due to two more current sheets at $y = 3L_y/2$ and $y = -3L_y/2$ (outside of the simulation box). This is a small correction due to the periodic boundary conditions introduced to account for the exponential tail that passes through the boundary.

This current-sheet setup is unstable to the tearing instability, which grows naturally from the particle noise without externally imposed seed fields. In order to facilitate the onset of magnetic reconnection, the initial thickness of the current sheet δ is chosen to be sufficiently small (of the order of the gyroradius of the particles in the sheet), so that the tearing instability growth rate approaches the characteristic cyclotron period (Daughton 1999). We normalize all the length scales in our simulations to $\rho_L \equiv \gamma_T m_e c^2 / e B_0 = \gamma_T c / \Omega_c$, defined as the Larmor radius of a background particle with a Lorentz factor corresponding to the peak of the initial upstream relativistic Maxwell-Jüttner distribution, $\gamma_T \equiv 2T_b/m_e c^2$, and choose $\delta > \rho_L$, ρ_{L0}, where $\rho_{L0} = \rho_L T_0 / T_b$ is the gyroradius of a typical particle in the current sheet.

The three main physical parameters that describe the upstream plasma conditions outside of the current sheets – T_b, n_b, and B_0 – define two important dimension-less parameters: the magnetization σ_h and the plasma-β parameter, β_{up} (the ratio of the background plasma pressure to the magnetic pressure):

$$\sigma_h \equiv \frac{B_0^2}{4\pi (2n_b) h_b}, \tag{A3}$$

$$\beta_{up} \equiv \frac{8\pi (2n_b) T_b}{B_0^2} = \frac{2T_b}{h_b} \frac{1}{\sigma_h}. \tag{A4}$$

The subscript h refers to the 'hot' magnetization σ_h, defined with the upstream background relativistic enthalpy per particle h_b (Melzani et al. 2013). In the non-relativistic limit ($T_b \ll m_e c^2$), the enthalpy $h_b \approx m_e c^2 + 5/2 T_b$ is dominated by the rest-mass $m_e c^2$ and so the 'hot' magnetization σ_h approaches the so-called 'cold' magnetization

$$\sigma_c \equiv \frac{B_0^2}{4\pi (2n_b) m_e c^2}, \tag{A5}$$

which is often used in the literature. In the ultrarelativistic limit ($T_b \gg m_e c^2$), however, $h_b \approx 4T_b$, and then $\sigma_h = 1/(2\beta_{up})$.

Using the β_{up} parameter allows us to cast the electron and positron drift speed inside the two Harris current layers, determined by Ampère's law, in a convenient form as

$$\frac{v_d}{c} = \frac{1}{\beta_{up}} \frac{\rho_L}{\delta} \frac{n_b}{n_0 - n_b}. \tag{A6}$$

In addition, the temperature T_0 of the drifting plasma in the layer, determined by the cross-layer pressure balance, can be written as

$$\frac{T_0}{m_e c^2} = \frac{T_b}{m_e c^2} \frac{\gamma_d}{\beta_{up}} \frac{n_b}{n_0 - n_b}, \tag{A7}$$

where $\gamma_d \equiv 1/\sqrt{1 - v_d^2/c^2}$. We can thus derive a convenient expression for the proper drift velocity $u_d = \gamma_d v_d/c$,

$$u_d = \frac{\rho_L}{\delta} \frac{T_0}{T_b} = \frac{\rho_{L0}}{\delta}. \tag{A8}$$

This shows that for constant values of δ/ρ_L and T_0/T_b, the drift u_d is also constant.

APPENDIX B: BOUNDARY FROM KINKING

As we pointed out in the histogram in Fig. 12, there exists a boundary in n-B space in the 3D case, that corresponds to a maximum value of n, or equivalently a minimum value of B, following the scaling

$$B_{min} \propto n. \tag{B1}$$

In this appendix, we will sketch a heuristic argument aimed at understanding the origin of this scaling and will discuss how the location of the limit is likely determined by unstable kinking modes that occur for regimes with large densities.

As we discussed in Section 3.2, the upstream background plasma is frozen into the magnetic field and follows equation (19). In the inner non-ideal (diffusion) regions near X-points, where magnetic reconnection takes place, the frozen-in condition is broken, and the plasma density may move to new regions of n-B space. Once the plasma and the associated reconnected magnetic flux escape from the X-point regions and join nearby circularized magnetic islands (magnetic flux ropes in 3D), the frozen-in condition holds again. In the outer regions of these flux ropes, assuming that the background guide magnetic field is weak, the magnetic field strength is dominated by the in-plane, reconnected component B_{xy}, and the ideal-MHD

evolution of a given fluid element in the n-B space follows equation (20) (see Section 4.2). Then, however, as the flux rope grows further on the outside by accumulating more and more reconnected flux and by merging with other flux ropes, the given fluid element gets buried deeper and deeper inside the flux rope and experiences compression. The magnetic flux also compresses, but this compression has a greater effect on the out-of-plane (guide) magnetic field component B_z, which thus eventually comes to dominate over B_{xy} deep inside the flux rope's core. As long as ideal MHD holds in this region during this compression process (i.e. the rope's core radius is much greater than the typical particle gyroradius, and the radiative resistive effects, discussed in the next two appendices, can be neglected), and before any 3D instabilities, such as the kink, get excited and cause mixing of plasma, the joint evolution of the plasma density and the guide magnetic field B_z (which dominates in these regions) follows the scaling equation (B1). Since the central cores of these flux ropes/ current filaments are also the highest density regions, their behaviour determines the slope of the high-n compression boundary.

Up to this point, the above discussion was applicable to both 2D and 3D cases. However, in 2D, the density and magnetic field remain relatively constant at the centre of plasmoids (i.e. regions where $n/n_b > 10$). These regions, therefore, do not occupy much area in n-B space, as was shown in Fig. 6, and thus do not result in a clear power-law high-n boundary. In contrast, in 3D, these quantities evolve and fill the n-B space, in part because of the freedom of motion of plasma along the third dimension.

We believe that the slope and the location of this boundary in 3D are governed by the marginal stability condition of the compressed current-filament (flux-rope) cores to the kink instability. Approximating these flux ropes as simple cylindrical pinches, we can invoke the well-known Grad–Shafranov (GS) criterion for the instability onset, cast in terms of the safety factor q:

$$\frac{1}{q(r)} \equiv \frac{B_{xy}}{B_z} \frac{\ell_z}{r} > 1. \tag{B2}$$

Here, r is the cylindrical radius inside the flux rope's core, ℓ_z is its length in the z-direction, $B_{xy}(r)$ is the in-plane magnetic field, and B_z is the out-of-plane (guide) magnetic field inside the flux rope.

In the following, we shall assume that inside each flux-rope core, the out-of-plane magnetic field B_z and the current density j_z are approximately uniform in r. The in-plane magnetic field as a function of radius r inside a given core can then be estimated using Ampere's law as

$$B_{xy}(r) \simeq \frac{2\pi j_z}{c} r, \tag{B3}$$

i.e. increases linearly with the radius inside the flux rope. This is important because, once this expression for the in-plane magnetic field is plugged into the GS instability condition (B2), the radius r cancels, and the condition becomes

$$\frac{1}{q} = 2\pi \ell_z \frac{j_z}{c} \frac{1}{B_z} > 1. \tag{B4}$$

Next, it is reasonable to assume that the guide magnetic field B_z dominates over (or is at least comparable to) B_{xy} inside plasmoid cores, and thus provides a good estimate for the total magnetic field strength B there. Furthermore, we shall assume that counterstreaming (in z) electrons and positrons contribute equally to the current density in the z-direction, so that $j_z = 2env_d$, where n is the density of the electrons (or positrons, which we will assume is equal) in the plasmoid core and $v_d = \beta_d c$ is the absolute value of the drift z-velocity of the current-carrying particles. For simplicity, we shall view both n and v_d as being uniform inside a given plasmoid core.

We can then recast the marginal kink stability condition $q = 1$ for a given flux-rope core in terms of a linear relationship between the magnetic field $B \approx B_z$ and density n inside of it as

$$\frac{B}{n} \simeq 4\pi e \, \ell_z \, \beta_d \, . \tag{B5}$$

We can go one step further and express this relationship in terms of the dimension-less, normalized density and magnetic field, n/n_b and B/B_0, that form the axes of our 2D n-B histograms. We then get

$$\frac{B/B_0}{n/n_b} \simeq \frac{1}{2\sigma_c} \frac{\ell_z}{\rho_0} \beta_d, \tag{B6}$$

where $\sigma_c \equiv B_0^2/(8\pi n_b m_e c^2)$ is the initial upstream 'cold' magnetization [corresponding to the total, electron plus positron, particle density $2n_b$, see equation (A5)] and $\rho_0 \equiv m_e c^2/eB_0$ is the nominal relativistic Larmor radius. The cold magnetization provides the basic scale for the available upstream magnetic energy per particle, and then the combination $\rho_c \equiv \sigma_c \rho_0$ gives the corresponding characteristic Larmor radius of reconnection-energized particles. For a relativistically hot upstream plasma, $\sigma_c = 4\sigma_h(T_b/m_e c^2) = 2\gamma_T \sigma_h$, and hence

$$\rho_c \equiv \sigma_c \rho_0 = 2\sigma_h \rho_L \, . \tag{B7}$$

Thus, the kink-based density boundary can be written as

$$\frac{B/B_0}{n/n_b} \simeq \frac{\ell_z}{2\rho_c} \beta_d = \frac{1}{4\sigma_h} \frac{\ell_z}{\rho_L} \beta_d \, . \tag{B8}$$

Note that σ_h and ρ_L appearing in the expression on the right-hand side are just fixed parameters, defined in terms of the initial upstream plasma conditions; they are, therefore, constant, by definition, within a given simulation. Thus, in order to see whether the $B \sim n$ scaling (B1) for the high-density histogram boundary holds, one just needs to examine β_d and ℓ_z.

Empirically, in our simulations we see that different plasmoid cores reach roughly similar typical peak values of $\beta_d \simeq 0.2$, with relatively little variation.

As for estimating the relevant values of ℓ_z, one can consider two arguments. First, the upper limit on ℓ_z is given by the z-extent of the computational box: $\ell_z = 2L_z$. Then, all the quantities on the right-hand side of equation (B8) have fixed (i.e. the same for all flux-rope cores) values for a given simulation, and we thus recover the high-n histogram-boundary scaling (B1), i.e. $B \sim n$. Quantitatively, for our fiducial simulations with $\sigma_h = 25.76$ and $2L_z = 117\rho_L$, we obtain

$$\frac{B/B_0}{n/n_b} \simeq \beta_d \simeq 0.2 \, , \tag{B9}$$

which agrees reasonably well with the location of this boundary for both radiative and non-radiative cases as can be seen in Figs 12(a) and (b).

Alternatively, one can argue that kink modes that are particularly effective in disrupting the compression of a flux rope and causing efficient plasma mixing, are those with their z-wavelength, ℓ_z, comparable to, but perhaps somewhat longer (but not much longer) than, the flux-rope core's diameter $2r$. The GS condition equation (B2) is then roughly equivalent to $B_{xy} \sim B_z/2$ (c.f. Pritchett & Coroniti 2004). We observe that in our 3D simulations, compressed flux-rope cores have characteristic radii[2] of $r \sim 20\rho_L$, and hence further compression is disrupted by kink modes with $\ell_z \sim 40\rho_L$. Substituting

---

[2] See e.g. Fig. 11; note that Fig. 11 shows an earlier time, $tc/L_y = 1.5$, whereas the histogram in Fig. 12 is at a later time, $tc/L_y = 3$. While the flux ropes do become larger over time, the relevant cores remain about the same size.

this estimate into equation (B8), we get, for our fiducial $\sigma_h = 25.76$ case,

$$\frac{B/B_0}{n/n_b} \simeq \frac{10}{\sigma_h} \beta_d \simeq \beta_d/2.5 \simeq 0.08 \, . \tag{B10}$$

This provides an excellent fit for the boundaries in Figs 12(a) and (b) and in Fig. 14(a).

After the kink instability gets excited and mixes high- and low-density regions, we expect the density to be limited to the stable regions in n-B space, such that the boundary occurs at marginal stability given by the above condition, as we discussed in Section 5.2.

APPENDIX C: EFFECTIVE RADIATIVE RESISTIVITY DERIVATION

In this appendix, we derive an expression for the effective radiative resistivity $\eta_{\rm eff}$, which acts in a manner similar to the standard collisional *Spitzer* resistivity (Spitzer & Härm 1953; Krall, Trivelpiece & Kempton 1973) in the magnetic induction equation. This radiative dissipation is caused by the synchrotron radiation reaction instead of binary particle collisions.

Just like with the collisional resistivity, the radiative resistivity can be formulated for an arbitrary orientation of the electric field relative to the magnetic field. In the case when the two fields are not strictly aligned (or anti-aligned), the perpendicular component of the electric field drives an $\boldsymbol{E} \times \boldsymbol{B}$ drift of the magnetic field lines; in the case of a resistively decaying magnetic flux rope with an azimuthal magnetic field and an axial electric field, this drift is directed inwards, towards the rope's centre. However, if the electric force on the electron (or positron) fluid is balanced by the net radiation-reaction force $\boldsymbol{F}_{\rm rad}$, then the $\boldsymbol{E} \times \boldsymbol{B}$ drift of the particles is cancelled by the oppositely directed drift due to the radiative friction force. The resulting resistive slippage of the plasma particles relative to the inward-drifting magnetic field lines allows the plasma in a flux-rope core to remain approximately static while the azimuthal magnetic flux moves inward and eventually gets destroyed at the flux rope's O-point.

In order to obtain a simple estimation for the synchrotron radiative resistivity quantifying this resistive slippage, we will make a few assumptions. First, we shall assume that the electron and positron populations move in opposite directions in response to a superimposed electric field $\boldsymbol{E} = E\hat{\boldsymbol{x}}$, contributing equally to the resulting electric current (i.e. the net e^+e^- flow is zero). We shall also assume for simplicity that the electron and positron distributions $f_{e,p}(\boldsymbol{u})$, where $\boldsymbol{u}$ is the normalized momentum (proper velocity normalized to c), can be approximated by two drifting ultrarelativistic Maxwell-Jüttner distribution functions with the same density n and normalized temperature $\Theta_e \equiv T_e/m_e c^2 \gg 1$. The distributions are boosted along the flow ($\hat{x}$) direction by a drift velocity $c\boldsymbol{\beta}_d = \pm c\beta_d\hat{\boldsymbol{x}}$ (where the '+' sign is for positrons and '−' sign is for electrons), corresponding to a drift Lorentz factor $\gamma_d \equiv (1 - \beta_d^2)^{-1/2} \sim 1 \ll \theta_e$. In this Appendix, we ignore any possible spatial dependence of our quantities.

The standard way to formulate a resistivity is to calculate, in a steady state, how much electric current can be driven by an externally imposed electric field $\boldsymbol{E}$, taking into account the presence of friction on the charge-carrying particles. The steady state is then determined by balancing the total volumetric electric force on one of the species, e.g. the electrons, with the volumetric friction force, which, in the case under consideration here, is the radiation-reaction force per unit

volume, $\boldsymbol{F}_{\rm rad}$. Thus, for electrons,

$$-en\boldsymbol{E} = -\boldsymbol{F}_{\rm rad} = -\int \mathrm{d}^3 u\, f_e(\boldsymbol{u})\, \boldsymbol{f}_{\rm rad}(\boldsymbol{u}), \tag{C1}$$

where the synchrotron radiation-reaction force on an ultrarelativistic particle is

$$\boldsymbol{f}_{\rm rad}(\boldsymbol{u}) = -\frac{2}{3}\,\boldsymbol{\beta}\,\frac{(\boldsymbol{B}\times\boldsymbol{u})^2 e^4}{m_e^2 c^4} = -2\,\sigma_T\,\frac{B^2}{8\pi}\,\boldsymbol{\beta}\, u^2 \sin^2\alpha\,. \tag{C2}$$

Here $\boldsymbol{\beta} \equiv \boldsymbol{u}/\gamma$ is the particle's 3-velocity, α is its pitch angle with respect to the magnetic field $\boldsymbol{B}$, and $\sigma_T \equiv (8\pi/3)\, r_e^2 = (8\pi/3)\, e^4/m_e^2 c^4$ is the classical Thomson cross-section, $r_e \equiv e^2/m_e c^2$ being the classical electron radius.

Substituting equation (C2) into equation (C1), we get

$$-en\boldsymbol{E} = 2\sigma_T\,\frac{B^2}{8\pi}\int \mathrm{d}^3 u\,\boldsymbol{\beta}\,\frac{(\boldsymbol{B}\times\boldsymbol{u})^2}{B^2}\,f_e(\boldsymbol{u})\,. \tag{C3}$$

If we consider a set of coordinates where the applied electric field and the current are along the $\hat{\boldsymbol{x}}$ direction and the magnetic field is in the x–y plane, we can then express the x-component of the integral in equation (C3) as

$$\int \mathrm{d}^3 u\,\beta_x \left[u_x^2 \sin^2\theta + u_y^2 \cos^2\theta + u_z^2\right] f_e(\boldsymbol{u})\,, \tag{C4}$$

where θ is the angle between the current and the magnetic field, and where we made use of the assumption that the distribution function $f_e(\boldsymbol{u})$ is even with respect to u_y. For an ultrarelativistically hot plasma with $\Theta_e \gg 1$, we can evaluate the relevant integrals over the assumed boosted Maxwell-Jüttner electron distribution as follows:

$$\int \mathrm{d}^3 u\,\beta_x u_x^2\, f_e(\boldsymbol{u}) \simeq -12\, n\Theta_e^2\, \beta_d \left(1 + 2u_d^2\right)\,, \tag{C5}$$

and

$$\int \mathrm{d}^3 u\,\beta_x u_y^2\, f_e(\boldsymbol{u}) = \int \mathrm{d}^3 u\,\beta_x u_z^2\, f_e(\boldsymbol{u}) \simeq -4\, n\Theta_e^2\, \beta_d\,, \tag{C6}$$

where the negative sign appears because the electrons are boosted in the direction opposite to the current. Then, equation (C3) becomes:

$$-en\boldsymbol{E} \simeq -16\, n\sigma_T\,\frac{B^2}{8\pi}\,\Theta_e^2\,\beta_d \left[1 + (1 + 3u_d^2)\sin^2\theta\right]\hat{\boldsymbol{x}}\,. \tag{C7}$$

One can now solve for the electric field in terms of the current density generated by both the electrons and positrons $\boldsymbol{j} = 2en\beta_d c\,\hat{\boldsymbol{x}}$:

$$\boldsymbol{E} \simeq 8\,\frac{\sigma_T}{cne^2}\,\frac{B^2}{8\pi}\,\Theta_e^2 \left[1 + (1 + 3u_d^2)\sin^2\theta\right]\boldsymbol{j}\,. \tag{C8}$$

Comparing with Ohm's law, $\boldsymbol{E} = \eta\boldsymbol{j}$, we thus find an effective radiative resistivity $\eta_{\rm eff}$:

$$\begin{aligned}\eta_{\rm eff} &\simeq \frac{\sigma_T}{cne^2}\,\frac{B^2}{\pi}\,\Theta_e^2 \left[1 + (1 + 3u_d^2)\sin^2\theta\right]\\ &= \frac{64}{3}\pi\,\frac{r_e}{c}\,\sigma_c\,\Theta_e^2 \left[1 + (1 + 3u_d^2)\sin^2\theta\right]\,,\end{aligned} \tag{C9}$$

where $\sigma_c = B^2/8\pi nm_e c^2$ is the cold magnetization based on the local values of the magnetic field and total particle density $2n$. For simplicity and since the expression in equation (C9) only varies by a factor of about 2 when varying the angle θ (assuming $\gamma_d \sim 1$), let us average over θ assuming a uniform, isotropic distribution of these

angles in 3D space. This isotropic average leads to the estimate:

$$\begin{aligned}\eta_{\rm eff} &\simeq \frac{\sigma_T}{cne^2}\,\frac{B^2}{\pi}\,\Theta_e^2 \left(\frac{5}{3} + 2u_d^2\right)\\ &= \frac{8}{3}\,\frac{e^2 B^2}{nm_e^2 c^5}\,\Theta_e^2 \left(\frac{5}{3} + 2u_d^2\right)\\ &= \frac{64}{3}\pi\,\frac{r_e}{c}\,\sigma_c\,\Theta_e^2 \left(\frac{5}{3} + 2u_d^2\right)\,.\end{aligned} \tag{C10}$$

This effective radiative resistivity can act as a dissipative term in the resistive-magnetohydrodynamics (MHD) magnetic induction equation,

$$\frac{\partial \boldsymbol{B}}{\partial t} = -c\,\nabla\times\boldsymbol{E} = \nabla\times(\boldsymbol{v}\times\boldsymbol{B}) - \nabla\times\left[\frac{\eta_{\rm eff} c^2}{4\pi}\,\nabla\times\boldsymbol{B}\right]\,, \tag{C11}$$

resulting in a simple expression for the radiative magnetic diffusivity:

$$\frac{\eta_{\rm eff} c^2}{4\pi} \simeq \frac{16}{3}\,cr_e\,\sigma_c\,\Theta_e^2 \left(\frac{5}{3} + 2u_d^2\right) \approx \frac{80}{9}\,cr_e\,\sigma_c\,\Theta_e^2\,, \tag{C12}$$

where the last expression is valid for small u_d.

Note that all the quantities appearing in the expressions presented in this appendix, e.g. B, n, Θ_e, β_d, γ_d^2, and σ_c, are local, and so their values may, in general, be different from the globally defined initial system parameters that are used elsewhere in the paper.

APPENDIX D: RADIATIVE DISSIPATION BOUNDARY

In addition to the right boundary of the n-B histogram shown in Fig. 12, which we discussed in Appendix B, we can offer an explanation for the upper limit in the n-B space for the radiative cases, especially promising for the 3D radiative case. We empirically find a very shallow power law of $B \sim n^{1/12}$ which can be seen in both classical and radiative 3D cases [see Figs 12(a) and (b)]. However, in the radiative case [Fig. 12(b)], we also observe a somewhat steeper upper boundary at lower densities, $n \lesssim 2n_b$, consistent with the power-law scaling $B \sim n^{1/6}$. In this appendix, we will argue that this upper limit on the magnetic field strength is due to the radiative-resistive dissipation of the magnetic field in the central cores of secondary plasmoids filled with low-density background plasma from the upstream region.

To understand the radiative dissipation of magnetic flux ropes (current filaments), we first consider resistive decay described by the resistive-MHD magnetic induction equation (C11). In the collision-less relativistic plasmas under consideration in this study, the usual collisional resistivity can be neglected, but the effective radiative resistivity $\eta_{\rm eff}$ due to synchrotron radiation reaction, introduced in Appendix C, needs to be considered. The dissipation time-scale t_d can be obtained by comparing the left-hand side of equation (C11) with the second (diffusive) term on the right-hand side, yielding

$$\frac{1}{t_d} \sim \frac{\eta_{\rm eff} c^2}{4\pi r_{\rm var}^2}\,, \tag{D1}$$

where $r_{\rm var}$ is the gradient length scale of the magnetic fields in current filaments. Using our estimate (C9) for the effective radiative resistivity derived in Appendix C, we can express the corresponding radiative-resistive decay rate, normalized to the global light crossing time L_y/c, assuming $u_d \ll 1$, as

$$\frac{L_y}{ct_d} \sim \frac{80}{9}\,\frac{L_y r_e}{r_{\rm var}^2}\,\sigma_{c,\rm loc}\,\Theta_{e,\rm loc}^2\,, \tag{D2}$$

where we have added the additional subscript 'loc' in $\sigma_{c,\text{loc}}$ and $\Theta_{e,\text{loc}}$ in order to distinguish these local quantities, describing a given flux-rope core, from the globally defined initial parameters describing the simulation setup such as $\gamma_T = 2T_b/m_e c^2$.

This expression for the normalized radiative magnetic decay rate can be conveniently recast in terms of our simulation parameters as

$$\frac{L_y}{ct_d} \sim \frac{80}{9}\,\alpha_{\text{fs}}\,\gamma_T^{-1}\,\frac{L_y}{\rho_L}\frac{\rho_L^2}{r_{\text{var}}^2}\frac{B_0}{B_Q}\,\sigma_{c,\text{loc}}\,\Theta_{e,\text{loc}}^2 \propto \frac{B^2 T^2}{n}. \tag{D3}$$

The last expression represents the scaling of the normalized radiative-resistive dissipation rate with the local quantities (B, n, and T) used in our histograms from Section 3.2. Note that here we used

$$\sigma_{c,\text{loc}} \equiv \frac{B^2}{8\pi n m_e c^2} = 2\sigma_h \gamma_T \frac{B^2}{B_0^2}\frac{n_b}{n} \propto \frac{B^2}{n}, \tag{D4}$$

where σ_h, γ_T, B_0, and n_b are the initial upstream plasma parameters introduced in Section 2.

Similarly, we define a radiative cooling time t_{cool} as the time for a typical (thermal) particle with energy $\gamma = 2\Theta_{e,\text{loc}}$ (corresponding to the peak of the relativistic Maxwellian distribution), gyrating perpendicular to the local magnetic field B, to lose an order-unity fraction of its energy to synchrotron cooling. The ratio of the light crossing time to the cooling time can be written as

$$\frac{L_y}{ct_{\text{cool}}} = \frac{4}{3}\,\alpha_{\text{fs}}\,\frac{B_0}{B_Q}\frac{L_y}{\rho_L}\frac{B^2}{B_0^2}\,\Theta_{e,\text{loc}}\,\gamma_T \propto B^2 T. \tag{D5}$$

Again, the last expression is the scaling with respect to the space-dependent parameters used in our histograms from Section 3.2. In our radiative case, $L_y/ct_{\text{cool}} = 0.44$ based on the background conditions T_b and B_0, and $L_y/ct_{\text{cool}} = 0.77$ for the initial Harris sheet conditions T_0 and B_0. While these values correspond to only moderate cooling of the initial plasma throughout the simulation, for the hot plasma energized by the reconnection process, especially in plasmoid cores, the cooling rate can be quite significant.

If the cooling rate $1/t_{\text{cool}}$ in a given region is slow compared to the magnetic field resistive dissipation rate $1/t_d$, then there is enough time for the magnetic field to decay before the plasma cools significantly. This ratio can be expressed as:

$$\frac{t_{\text{cool}}}{t_d} = \frac{20}{3}\sigma_h \frac{T}{T_b}\frac{n_b}{n}\frac{\rho_L^2}{r_{\text{var}}^2}. \tag{D6}$$

We believe that the magnetic field indeed suffers radiative-resistive dissipation in certain localized regions in the parameter regime of this present paper. As shown in Section 5.2, the magnetic field strength in regions with density $n/n_b \lesssim 2$ seems to be limited by the power-law boundary $B \sim n^{1/6}$. For the low-density secondary plasmoids in the 3D case, where $r_{\text{var}}/\rho_L \simeq 7$, $n/n_b \simeq 2$, $B/B_0 \simeq 1.5$, $T/T_b \simeq 1$, and $\gamma_{d,\text{loc}} \simeq 1$, we find the ratios $L_y/ct_d \simeq 1.8$ and $L_y/ct_{\text{cool}} \simeq 1$ (i.e. $t_{\text{cool}}/t_d \simeq 1.8$). Therefore, there is marginally enough time for the magnetic dissipation to become important and limit the compression of the magnetic field. In the 2D case, the parameters are about the same, and thus magnetic dissipation should also play a role in limiting magnetic field amplification. However, in this case, we do not observe the very clear boundaries in n-B space found in 3D to help confirm this hypothesis.

When, for a given flux-rope core, the normalized resistive dissipation rate (D3) exceeds unity (and at the same time also exceeds the normalized radiative cooling rate, $t_d < t_{\text{cool}}$), the magnetic field has sufficient time to dissipate within a light-crossing time (i.e. the flux rope's characteristic dynamical lifetime, enough time for a power-law boundary in n-B space to develop). The magnetic field's amplification by compression is then checked by the effective radiative-resistive decay. To evaluate the location of the corresponding histogram boundary in n-B space, we will assume, based on the numerical observation from Fig. 12(d), that $T \sim n^{1/3}$, a scaling that is expected from simple adiabatic compression for a relativistic plasma. As we have argued above, it is justifiable to ignore radiative cooling in these regions because the radiative-resistive decay of the magnetic field occurs faster than the cooling of the plasma. This adiabatic temperature scaling was also confirmed by checking the average local temperature at the boundary in n-B space for $n \lesssim n_b$ (not presented), giving a value of $\Theta_{e,\,loc} \approx 5(n/n_b)^{1/3}$, just slightly hotter than a scaling based on the initial background temperature $T_b = 4m_e c^2$ at $n = n_b$. Then, substituting the $T \sim n^{1/3}$ scaling into equation (D3), and setting the normalized resistive dissipation rate to be constant and of order unity, we obtain the scaling for the maximum magnetic field,

$$B_{\max} \sim n^{1/6}. \tag{D7}$$

This scaling provides a good match with the upper boundary of the n-B histogram observed in Fig. 12(b).

This paper has been typeset from a TeX/LaTeX file prepared by the author.